Doctoral Dissertation (Censored)

博士論文(要約)

Data-driven approach and numerical simulation for reproduction and measurement of complex fluids

（データ駆動的アプローチと数値計算による複雑流体の再現と計測）

A Dissertation Submitted for the Degree of Doctor of Philosophy

December 2021

令和 3 年 12 月博士 (理学) 申請

Department of Physics, Graduate School of Schience,

The University of Tokyo

東京大学大学院理学系研究科 物理学専攻

Kentaro Nagasawa

永澤　謙太郎

ABSTRACT

In this thesis, we perform the analyses related to the reproduction and measurements of various fluids classified as a complex fluid having interesting properties, solid-like behavior, and nonlinear viscosity, e.g., sauces, creams, and pastes from the perspective of micro or macro, by effective use of the data-driven approach and the numerical simulation.

A wide variety of fluids can be seen around us in various fields and regions, such as food production, daily commodities, biological body, and natural landscape. We make use of these in our daily lives by measuring, reproducing, and understanding their physical property. There are simple fluids with constant viscosity in the fluids around us, e.g., water and honey. However, some fluids have more interesting properties. For example, viscosity nonlinearly changed depending on the shear rate related to the flowing velocity (e.g., sauce, lubricant) and behaving like a solid (e.g., cream, form). These characteristic phenomena, which are nonlinear viscosity and solid-like behavior, are known to be due to some inclusion of internal elements such as colloids and polymers in the fluid, and these fluids are categorized as complex fluids. We will focus on the nonlinear viscosity and solid-like properties as the characteristic properties of complex fluids to be analyzed and investigate the reproducing and measurements for these properties.

In analyzing the complex fluids, the parts that can be simplified and coarse-grained are modeled and then reproduced using numerical simulation. On the other hand, when the internal structure or mechanism is an unknown or a black box, a data-driven fitting approach is used. In this thesis, these two approaches, the numerical simulation and the data-driven approach, are smartly used for the target to be analyzed, we thus would like to obtain new knowledge and methods for handling more complex fluids. It also aims to investigate the knowledge and methodologies that can be applied to as broad a class of complex fluids as possible, rather than limiting the class of fluids with certain internal elements, structures, and properties.

In the context of reproducing the solid-like behavior, we explored the limits of reproducing the solid-like behavior of complex fluids and the uncleared physical behavior occurring around them. It is well known that the existence of solid-like behavior, in a form and paste, is due to the jamming transition phenomenon, which depends on the density of particles as internal elements in the fluid. The Reversible-Irreversible (RI) transition, which is related to the reversibility of particle trajectories in the oscillatory sheared system, has been reported to be qualitatively different in the high-density and low-density regions, implying a connection with the jamming phenomenon. In this thesis, a numerical simulation of a simple particle system as an athermal colloidal suspension was performed under various density conditions around the jamming transition density and shear amplitude to obtain exhaustive data. We obtained a phase diagram covering the intermediate density region for the RI transition and the relationship between the RI transition and solid-like behavior from these data. We also observed the existence of non-trivial RI transitions and nonlinear elastic behavior in the region below the jamming density, indicating the existence of a richer physical property. In addition, we found that the RI transition and solid-like behavior are related and can be described by the contact number reflecting the mesoscopic structure of the particle system.

In the context of reproducing the nonlinear viscosity, we aim to find a method for reproducing and estimating the nonlinear viscosity of the complex fluid mixture, including various classes of fluids mixture as possible, irrespective of the internal elements and the structure. From a macroscopic perspective, we can consider the complex fluid with disorder internal elements as a homogeneous fluid with a (nonlinear) flow curve representing the physical property of flowing.

We observed that the Harshall-Bulkley model could represent the flow curves of various pure fluids and their mixtures. Hence, as a blending model that reproduces the physical properties of mixtures, we considered a new model that reproduces the physical properties of mixtures from the physical properties of individual pure fluids and the mixing ratio, which is closed by the parameters of the Harshall-Bulkley model. In order to consider the blending model, we introduced the laws of blending and a general blending model satisfying these laws. Using a data-driven approach, we chose the proposed model. We showed that the model exists that can qualitatively reproduce the characteristic behavior of a mixture of various fluids combinations within the general blending model. In addition, macroscopic simulations of mixtures were performed using our proposed model and compared with real experiments to verify the effectiveness of our model.

In the context of measuring the complex fluid, we proposed a video-based measurement method for conveniently measuring the flowing behavior of complex fluids that non-specialists can use. Although fluids with various and rich properties are very familiar to us, the method to measure with accurate them is not common because it requires a mechanical experimental device called a rheometer, which is expensive and needs expert knowledge. A physical property measurement corresponds to the inverse problem of the forward problem of reproducing a certain physical property. We interpret the existing video-based viscosity measuring method for Newtonian as a method based on the numerical solution of the inverse problem by combining a fluid simulation and optimization. Extending it to the complex fluids as the Herschel-Bulkley model, we proposed a method for estimating and measuring the flow curve of various classes of complex fluids from the experimental videos. In addition, we proposed a method to evaluate effective experimental setups to capture the fluid video for estimation and to select new setups. We validated the effectiveness of our method by using the artificial data and real data.

Contents

Chapter 1

Introduction

1.1 Diverse fluid and application

We observe diverse fluids around us in different fields, such as food, daily products, medical products, biological body, nature landscape, computer graphics. By measuring the properties of fluids, elucidating their mechanisms, and reproducing them, we are making use of these fluids in our daily lives [24]. Here are some practical examples.

Food is a typical example of fluid have various mechanical property and application [89], For example, the production of ketchup, it is necessary to produce ketchup of consistent quality every year, however, the properties of tomato puree, the raw material for ketchup, are not constant, as they are affected by the climatic conditions in different regions from year to year. Therefore, a mixture of several raw materials of tomato puree is used to adjust the quality to be consistent year after year [6]. The mouthfeel of food, such as "thickness", depends on the nonlinear fluid rheology [17]. In order to design the easily swallowing food product for the people who are difficulty swallowing, the analysis of flowing property is effective [68, 53].

It has been investigated how the texture and properties of creams and gels are affected by their internal elements and components [30]. It is necessary to change the components and elements that make up the fluid without changing the macroscopic functional properties of the cream, such as ease of application. Therefore, it is necessary to measure such functional quantities as physical quantities and design the internal elements.

Since natural phenomena such as landslides and avalanches have a significant influence on the infrastructure of our daily lives, it is necessary to predict whether they will occur and take countermeasures. By considering the geological landscapes as a complex fluid (particle-fluid mixture), understanding and linking to the mechanism of geological flow have been studied [41]. The analysis of the mechanism by which sediment yielding changes from a solid-like state to a fluid-like flowing state induced by an external force, such as vibration or impulsive force, is used in methodologies for disaster prediction [27, 36].

Fluids appear in various areas, and by understanding their properties, we can apply

them in our daily lives.

1.2 Having rich behavior of complex fluids

When we think of fluids, the first thing that comes to mind is a simple fluid, e.g., water or honey that has a constant viscosity and can change shape and flow freely. However, there are fluids that have richer properties [71]. For example, the viscosity of sauces in food products and lubricating oils in industrial products is not constant but decreases as the shear rate increasing. Foods such as margarine and jam, which are intended to be spread on bread, is effectively used of this shear-thinning effect. On the other hand, the fluid, e.g., dissolved corn starch at a constant rate, the viscosity will increase (rapidly) as the shear rate increases. Thus, some fluid have nonlinear viscosity.

A Cream, paste, and sediment have solid-like behavior, retaining their shape when at rest (under gravity) and exhibiting a reversible deformation response at small external forces, but when a large external force or impulsive force is applied to the object, they change their shape irreversibly and flow like a fluid.The mayonnaise and sauces can be dipped in vegetables, which is an example of effective use of the fact that the sauce adheres to the fluid.There are fluids that have solid-like properties.

These characteristic phenomena, which are nonlinear viscosity and solid-like behavior, are known to be due to some inclusion of internal elements such as colloids and polymers in the fluid, and these fluids are categorized as complex fluids. Although complex fluids have a more variety of properties [24] other than we introduced above, we will focus on the nonlinear viscosity and solid-like properties as the characteristic properties of complex fluids to be analyzed and investigate the reproducing and measurements of these properties.

1.3 Motivation and construction of the thesis

Our motivation; we do not desire to leave a fluid having complex structures and rich properties unknown and unmanageable. In order to measure, analyze, and reproduce such complex fluids, we handle the parts that can be modeled, internal elements modeling colloidal sphere or polymer chain as microscopic, and perform numerical simulations to this modeled system and exhaustive analyses. In contrast, data-driven fitting approaches have been used to deal with areas where the structure or mechanism is a black box. Even in the days of classical fluid mechanics, various insights and knowledge, such as the relationship between flow velocity and flowing area and the properties related to viscosity, were empirically derived from the accumulated data of observations and measurements by hydraulic engineers [13]. We smartly use these two approaches, numerical simulation and data-driven approach, for the target to be analyzed and obtain new insights and methods for handling more complex fluid objects. We also aim to obtain a more general understanding and methodologies that can be applied to as broad a class of complex

fluids as possible, rather than limiting to a class of fluids with specific structures and properties.

For complex fluids, there is a method of constructing a model from a microscopic view and reproducing macroscopic phenomena. On the other hand, explaining the phenomena only from the macroscopic view may make it possible to deal with more complex fluids. In this paper, we attempted to analyze a wide class of complex fluids by using the two perspectives, macroscopic or microscopic, depending on the purpose and target. The solid-like behavior is considered to be caused by jamming transition, which is a critical phenomenon related to the density of internal elements [20]. For this reason, we will perform a numerical simulation from a microscopic point of view to describe the solid-like and related properties. In nonlinear viscosity, it was difficult to identify the mechanism responsible for these properties because of various theories. We will treat the nonlinear viscosity from a macroscopic point of view. Because various complex fluids can be regarded as homogeneous systems regardless of their internal elements, and the material properties can be interpreted as nonlinear flow curves.

In Chapter 2, we described general models and methodologies for understanding the flowability of complex fluids from macroscopic and microscopic perspectives, and in Chapter 3, we described the simulation methods used in this thesis and the experimental device for measuring flowability.

In Chapter 4, we focused on the limit of reproducing solid-like behavior of complex fluids. We explore how the transition phenomena (RI transition), which is implied to relate to solid-like behavior, behave around the jamming transition density point by exhaustive numerical calculations and constructing a phase diagram of RI transition. The relationship between the mechanical behavior and the geometrical structure in the vicinity is also investigated.

In Chapter 5, we focused on the nonlinear viscosity and the reproduction of its change when various complex fluids are mixed. From a macroscopic point of view, we confirmed that the flowability of various complex fluids and their mixtures can be represented by the parameters of the Herschel-Bulkley model. Thus, we aimed to obtain a blending model that can estimate the physical properties of mixtures from the the physical property of pure fluids and their mixing ratios, using a data-driven approach.

In Chapter 6, we focused on the mismatch between the familiarity of various fluids and the unfamiliarity of their measurement, thus we aimed to develop a method that enables anyone to easily measure the physical properties of complex fluids. We proposed a method for estimating the physical properties of complex fluids from a video, effectively using of the fact that physical property measurements can be interpreted as inverse problems, and it can be solved numerically by combining numerical simulation and optimization.

In Chapter 7, we summarized and discussed these results

Chapter 2

Background

2.1 Macroscopic perspective of complex fluid

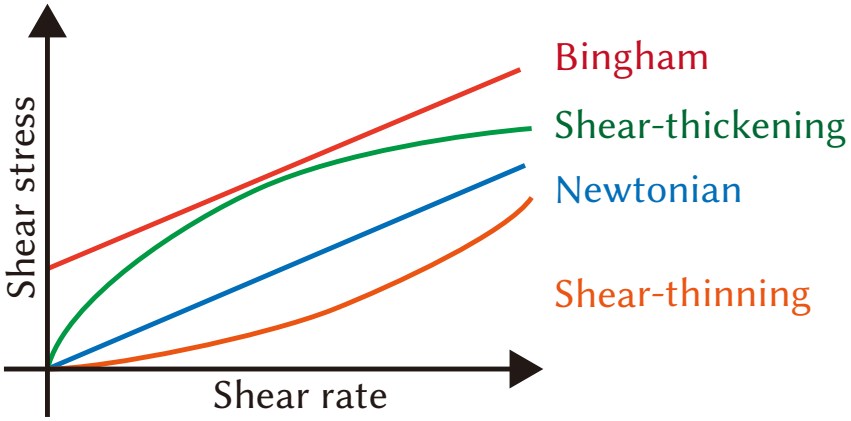

Figure 2.1: The schematic figure of flow curve.

Water, as the simplest fluid is flowing smoothly and splashing, while honey is flowing slowly and sticky. These differences can be characterized by viscosity, which is related to fluid flow resistance. However, if we look at the fluids around us, we will see more rich flowing behavior and property, e.g., sauces and creams in food products, foam and toothpaste in household products. These fluids have the non-constant viscosity dependent on flowing speed and keep their shape even when at rest.

From a macroscopic point of view, these flowing behavior of a fluid can be understood as the relationship between the shear stress σ_s and shear rate $\dot{\gamma}$, and this relationship is represented as a flow curve; the function of shear stress against shear rate $\sigma_s(\dot{\gamma})$ as shown in Fig. 2.1. Viscosity (effective viscosity), a popular measure of the flow resistance of a fluid, can be written $\sigma_s(\dot{\gamma})/\dot{\gamma}$ as the shear stress divided by the shear rate [1].

The physical properties related to the flowing behavior of various fluids can be represented by this flow curve. In the simple fluid called a Newtonian fluid, the flow curve is

[1] This definition is for effective viscosity, but for convenience, we will use the term as viscosity.

a straight line passing through the origin; the viscosity is a constant irrespective of shear rate, where the slope of the line shows a magnitude of viscosity. For example, water is a less viscous fluid, honey and syrup is highly viscous fluid.

In practice, more fluids do not actually belong to this Newtonian fluid class. When the flow curve is not a straight line, the viscosity is not a constant respective to the shear rate and can be considered as having a nonlinear viscosity. A convex upward curve indicates that the viscosity of the fluid decreases as the shear rate increases, this property is known as the shear-thinning behavior, e.g., most of the sauce for food, lubricant, paints. A convex downward curve indicates that the viscosity of the fluid increase as the shear rate increases, this property is known as the shear-thickening behavior. One of the famous examples is the oobleck which is a mixture of cornstarch and water.

If the flow curve does not pass through the origin and has a positive intercept, it takes on a finite shear stress when the shear rate is zero, i.e., a certain finite shear stress is required for the fluid starts to flow. This shear stress is called as a yield stress. This type of flow curve indicates that the fluid has a solid-like property with a finite yield stress, e.g., a form, cream, paste. Whether the fluid has a finite yield stress corresponds to the solid-like behavior. When applied to a small shear stress (below the yield stress), these materials behave like elastic materials, deforming in response to the load and recovering to their resting state when the load is removed. On the other hand, if a large shear stress (above the yield stress) is applied, the material yields and starts to flow. When the load is removed, the material no longer recovers its shape.

A model of flow curve

The flowing property of various fluids can be represented by the flow curve showing the relation between the shear stress and the shear rate. In practice, we use the rheometer to measure the shear stress at various shear rates, and we obtain the flow curve as a measurement point. Based on data and their fitting, several models that can represent the flow curve are known. These models can fit the measured data with several model parameters related to the flowing property [75].

The Newtonian model (2.1),

$$\sigma_s = \eta_N \dot{\gamma}, \tag{2.1}$$

represents the straight line passing through the origin and the Newtonian fluid, it has a constant viscosity η_N irrespective of the shear rate.

For the nonlinear flow curve, the power-low model (2.2),

$$\sigma_s = \eta_P \dot{\gamma}^{n_P}, \tag{2.2}$$

can fit the flow curve of power low behavior, this flow curve is linear in log-scale plot, where a constant parameter η_P is related to the entire consistency and a n_P is power

index ($n_P > 1.0$ shows shear-thickening, $n_P < 1$ shows shear-thinning, $n_P = 1$ reduced the Newtonian.)

For the fluid having solid-like property with a finite yield stress, The bingham model (2.3), the Kason model (2.4) and the Herschel–Bulkley model (HB model) (2.5) are known,

$$\sigma_s = \sigma_{BY} + \eta_B \dot{\gamma}, \tag{2.3}$$

$$\sqrt{\sigma_s} = \sigma_{CY} + \eta_C \sqrt{\dot{\gamma}}, \tag{2.4}$$

$$\sigma_s = \sigma_{HY} + \eta_H \dot{\gamma}^{n_H}. \tag{2.5}$$

These models can describe the yielding behavior, but they differ in their representation of the shear rate dependence of the flow. The Herschel–Bulkley model is more difficult to parameterize accurately experimentally than the Bingham and Casson models [67], but it is possible to fit a wide range of flow curve behaviors, and it reduces the bingham model (when $n_H = 1$), the power-low model (when $\sigma_{HY} = 0$), and the Newtonian model (when $n_H = 1, \sigma_{HY} = 0$). In the high shear region, Herschel–Bulkley model can most well fit the flow curves of solid-like fluid foods such as ketchup, mustard, and apple sauce [18]. Furthermore, it is known that Herschel–Bulkley model can represent a more wide range of fluids, such as concrete [37], debris flow [70], and fabric-water [58].

As for Fig. 3.4, we show the measured data by using the cone-plate or parallel-plate rheometer in (a) linear and (b) logarithmic scales. We can see many highly nonlinear curves, i.e., non-Newtonian fluid; their apparent viscosity depends on the shear rate, and it looks finite shear stress at a small shear rate in the logarithmic scale. In this thesis, we basically use the Herschel–Bulkley model model as a convenient model that can fit the fluid with a broad property of nonlinear viscosity and solid-like behavior.

2.2 Microscopic perspective of complex fluid

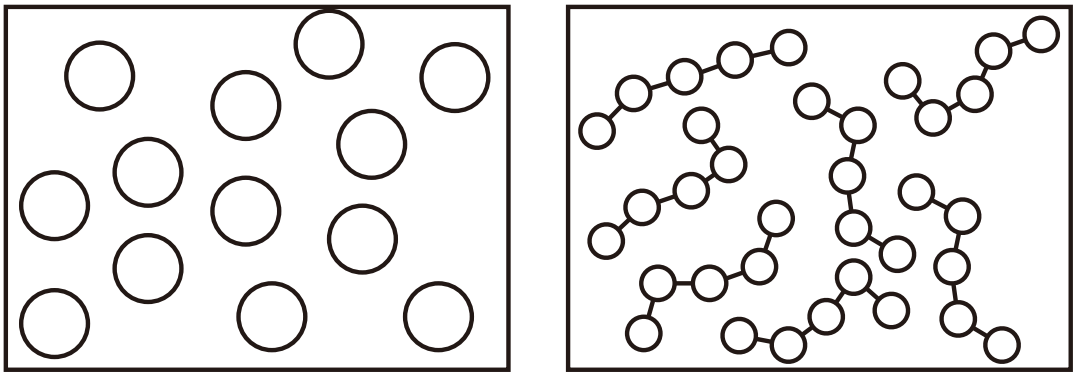

Figure 2.2: Schematic figures of a model of internal elements: (Left) colloidal suspension system, (Right) polymer solution system.

In the field of rheology, the mechanism of changes in nonlinear viscosity and solid-like behavior of fluids have been explained by modeling the internal components of the fluids, and the characteristic behavior is reproduced and applied through the analysis and numerical simulation of the modeled fluids.

The characteristic behavior, viscosity dependent on the shear rate, and solid-like behavior such as shape retention at rest state, can be due to the fluid having various internal elements complexities, e.g., particles and polymers dispersed and dissolved inside the fluid. A interaction between the internal elements and the fluid causes flow resistance related to viscosity. Moreover, each of the internal elements interacts with themselves and builds the structure (elements aligning to the same orientation, each element linking, and clustering) interacting with the fluid relating to the more rich fluid behavior [71]. Thus, its flow is characterized not only by the effects of its internal elements property but also by the effects of the combination of those internal elements, which enriches the flow behavior and the system. There are two main types of modeling of internal elements: colloidal suspensions system, in which solid (solid-like) particles are suspended in a fluid at a certain density, and polymer solutions system, in which polymers (particles connected in chains) are dissolved in the fluid. For each case, the flowing behavior has been discussed separately.

In the colloidal suspensions system, experiments and analyses have been conducted [64] on the phenomenon that viscosity changes and increases when solid particles are mixed and suspended in a background fluid, which is ideal viscous fluid, e.g., water. Einstein's viscosity equation [23] was derived analytically from considering the fluid flow around the particles,

$$\eta = (1 + B_e\varphi)\eta_0, \tag{2.6}$$

where η_0 is the viscosity of background fluid, φ is a volume fraction of particles, B_e is the Einstein's viscosity coefficient and $B_e = 2.5$ is derived by the Einstein. Batcher and Green extended this formula to the higher order of φ considering the contact of colloidal particles [64], $\eta = (1 + B_e\varphi + B_1\varphi^2)\eta_0$, where the coefficients is $B_1 \sim 5.2$. For colloidal suspension with the low-density volume fraction, the experimental results follow Einstein's viscosity equation (2.6), but in the more highly density colloidal suspension, Krieger-Dougherty equation [52] that can fit the experimental data of viscosity was proposed,

$$\eta = \left(1 - \frac{\varphi}{\varphi_J}\right)^{-2.5\varphi_J}, \tag{2.7}$$

where φ_J is the jamming transition density.

The φ_J is known as the density at which the jamming transition occurs, where the fluid starts to obtain the rigidity due to the close packing of particles. This jamming phenomenon is caused by the solid-like behavior of the complex fluid, and shows a critical behavior [20]. Jamming is considered to characterize the relationship between solid-like and fluid flowing behavior on a wide range of scales, from a small scales such as forms

and emulsions to a large scales such as sediments and avalanches [92]. Related to this jamming phenomenon, hydrodynamic analysis [81] of the shear thickening, in which the viscosity of a fluid increases rapidly depending on the shear rate, is performed. In addition, the relationship between the experimental results and the theoretical equations for flow behavior based on the density and size of the colloidal suspensions has been studied [35]. We will consider the Jamming is the key of the solid-like behavior of complex fluids and investigate in Section 4.

For an analysis using a model for polymer solutions, the polymer chain is described as a certain number of beads (solid particles) connected by a spring [19]. Based on calculating the Langevin equation, which corresponds to the equation of motion in the fluid of a certain length of beads, the Rouse model was proposed to discuss the viscosity and viscoelasticity of polymer solutions. The Rouse model does not consider entanglement, which is a many-body interaction with other polymers. De Gennes proposed the reptation model [16] to consider and discuss the entanglement of polymers and the mobility between polymers. Theoretical analysis and predictions of flow behavior and viscoelasticity of polymer solutions based on the reptation model were presented by Doi and Edwards [21, 22].

The existence of solid-like behavior, whether having elasticity, basically depends on the density of internal elements in the fluid related to the jamming transition as a critical phenomenon. In contrast to the solid-like behavior, the cause of nonlinear viscosity is considered various reasons due to the diversity of the internal elements; colloidal friction, fraction, inter-particle structure [8, 97, 51], orientation and microstructure entanglement [28, 48].

2.3 Approach to the more complex fluids in daily observed

Fluid that we observe in daily life, for example in the kitchen, we can see the various food, and cooking them via pouring, mixing, baking. In those fluids and that of process, the fluid internal elements and micro-structure is considered as more complex, e.g., existing colloids have various size and not spherical shapes as a fracture, thin cell, the polymer chained not straight but more complicated, or co-existing the those polymers and colloids. In addition, considering the fluid mixed with fluids have complex structure, those of internal structure depending on the mixing rate may be unknown. Therefore, it is not easy to represent them as micro models. Is it impossible to handle such a fluid, predict its viscosity, and reproduce its flowing behavior for analysis and application? We think that it is No, by considering these fluids from a different perspective, from a macroscopic point of view, we can deal with them. An example is the production of ketchup of quality control. A production company needs to control and produce ketchup of the same quality (flowing property) at all times. However, several pastes of tomatoes property, ingredient of ketchup, including various component such as broken soft sell, cell wall, and fracture having different size and shape, depends on the processing [79]

and the climate and soil of the regions where it is cultivated [90]. In order to treat such complex fluid, they consider these fluids from macroscopic property and make use of the experimental data, By controlling and optimizing the combinations of pastes of tomatoes with different properties and processing, they can obtain the desired material properties [6].

As we described, even fluids have more complex and disordered system that seem difficult can be handled by taking a macroscopic approach, considering it as a homogeneous fluid. Therefore, we believe that both microscopic and macroscopic approaches are important for understanding and applying the complex fluids of characteristic property. In Chapter 4, we will investigate the limit of the elastic property to approach the reproducing of the solid-like behavior from microscopic behavior. In Chapter 5, we will investigate the viscosity depending on the complex fluid mixing to approach the reproducing of the nonlinear viscosity behavior from macroscopic behavior. In Chapter 6, we will investigate a method to measure complex fluids conveniently by anyone to approach the measuring the flowing behavior from macroscopic behavior.

Chapter 3

Simulation and Measurement methods

3.1 Complex fluid Simulation method

We introduce the Material Point method (MPM) mainly for performing the simulation for complex fluid used in this thesis at the Chapter 5, and the Chapter 6.

3.1.1 Material Point Method

Sulsky et al. [87, 88] extended Particle-In-Cell (PIC) method to handle solid by introducing continuum mechanics and plastic mechanics. PIC is a simulation method that computes the hydrodynamic equation numerically with a hybrid technique, integrating with Eulerian grid and Lagrangian particle. In continuum mechanics, the material is considered continuum following continuity equation, dynamics is followed by Equation of Motion, and material property is defined constitutive equation. These three equations are called the governing equations, including the equations for fluids and elastic bodies. We consider that MPM is a hybrid simulation method for continuum mechanics. Based on continuum mechanics, particles track deformation gradient related to strain, which can compute the elastic part of the constitutive equation directly. Dividing deformation gradient into elastic and plastic parts introduced by mechanics of plasticity can represent plastic behaviors and flow. Because of the hybrid technique, we can simulate the free-surface dynamics, large deformation efficiently. These features of the MPM allow us to solve efficiently the governing equations involving the representation of various types of materials and phenomena; snow [84], powder as granular material [15, 32, 103, 49], form and cream as viscoelastic fluid [74, 102, 25, 86], cloth and knitt [42], fracture [101, 99], friction [54], surface tension [9], and phase transition [85, 9]. Simulating Multi-material interacting has been investigated, treating a multi phase flow [31, 73, 5, 26], an interacting and contact [40], and percolation [76]. Thanks to the capability of simulating various types of material in a single simulation scheme, MPM can simulate their interaction, coupling, mixing easily. fluid-solid two-way coupling is developed [26].

In order to perform more accurately and efficiently, the integrator part is also investigated. Original MPM has a problem about relatively large numerical viscosity and

dissipation caused by the hybrid method; information loss happens when the information on grid and particle is transferred. APIC [43], and PolyPIC [29] solve this problem and compute accurately by using the information of local velocity field when the information on grid and particle transferred. Hu et al. [40] showed that MLS-MPM can uniformly handle APIC and Poly-PIC on the single formulation.

To accelerate the calculating efficiency, Implicit time integration is adapted [25, 33]. Introducing Galerkin multigrid [95] GPU-based method has been investigated about efficiently computation with a tremendously large number of particle and scale [32, 96]. Now, MPM is a powerful tool for reproducing various materials including complex fluid, free-surface, accurate, efficient even on a large scale. MPM is used in not only computer graphics but also the science field. There are several investigations about snow avalanche with dynamic anticrack [34], and iceberg calving with large scale simulation [100].

3.1.2 Implementation of Material Point Method

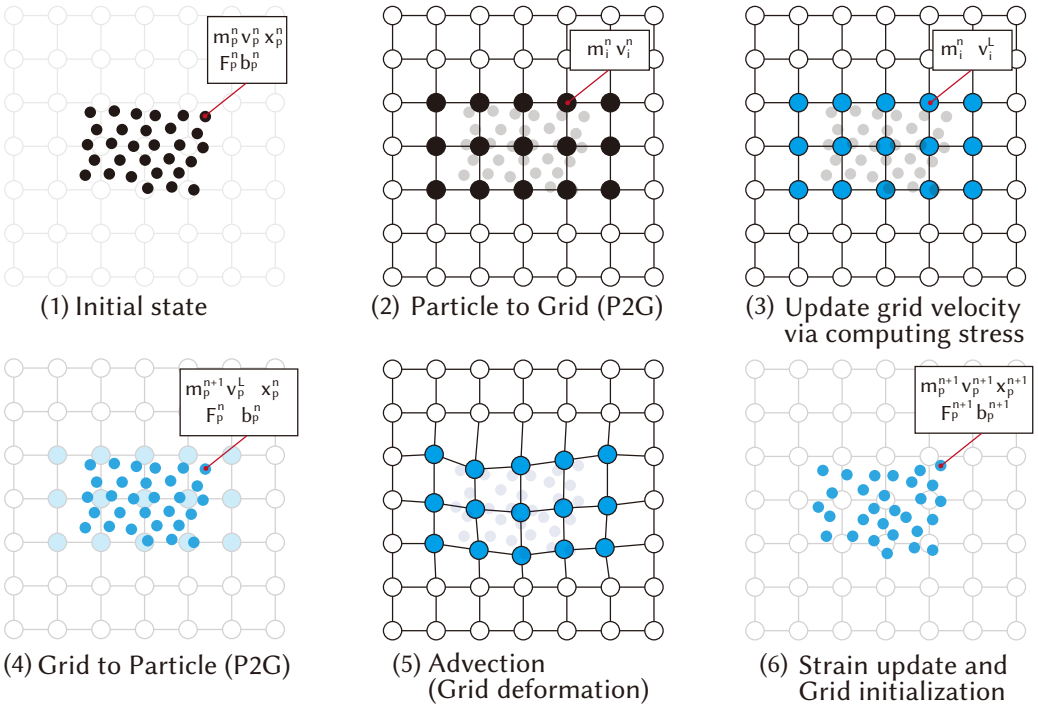

Figure 3.1: Schematic figure of material property updation via material point method.

In this thesis, we followed mainly the method of Sulsky et al. [87] and Yue et al. [102] to perform a MPM simulation for Herschel-Bulkley fluid. Fig. 3.1 shows the entire algorithm of material property integration. In addition, we applied APIC scheme [44] to reduce the information loss especially during a rotational motion.

Mass conservation and momentum conservation equations are

$$\frac{D\rho}{Dt} + \rho\nabla \cdot \boldsymbol{v} = 0, \tag{3.1}$$

$$\rho\frac{D\boldsymbol{v}}{Dt} = \nabla \cdot \sigma + \rho\boldsymbol{b} \tag{3.2}$$

where, $\rho = \rho(\boldsymbol{x}, t)$ is the mass density, $\boldsymbol{v} = \boldsymbol{v}(\boldsymbol{x}, t) = \frac{d\boldsymbol{u}(\boldsymbol{x},t)}{dt}$ is the velocity $\boldsymbol{u}$ is defined as the displacement, and $\boldsymbol{b}$ is the external force (body force). Note that we consider these equation in Lagrangian frame, thus the quantity $\boldsymbol{x} = \boldsymbol{x}(\boldsymbol{X}, t)$ is the current position at time t started from $\boldsymbol{X} = \boldsymbol{x}(\boldsymbol{X}, 0)$. $\boldsymbol{u} = \boldsymbol{u}(\boldsymbol{x}, t)$ is also can be defined as $\boldsymbol{u}(\boldsymbol{x}, t) = \boldsymbol{x} - \boldsymbol{X}(\boldsymbol{x}, t)$ ($\boldsymbol{X}(\boldsymbol{x}, t)$ is inversed function of $\boldsymbol{x}$).

Discretization of physical quantity on Grid and Particle

In order to solve these conservation equations, we discretized the physical quantity on Particle and Grid. In the particle side of discretization (Fig. 3.1(1)), the mass density can be written as a sum of point masses for representing particle located at $\boldsymbol{x}_p(t)$ of time t by using delta function $\delta(\boldsymbol{x})$

$$\rho(\boldsymbol{x}, t) = \sum_{p=1}^{N_p} m_p \delta(\boldsymbol{x} - \boldsymbol{x}_p(t)), \tag{3.3}$$

where N_p is the total number of point, m_p is the particle mass fixed.

In the grid side of discritization (Fig. 3.1(2)), we prepare spacial nodes $x_i(t)$ and standard nodal basis function $N_i(\boldsymbol{x})$ as representation of computational grid. Using spatial nodes $x_i(t)$ and nodal basis function $N_i(\boldsymbol{x})$, the coordinate $\boldsymbol{x}$ can be written as

$$\boldsymbol{x} = \sum_{i=1}^{N_n} \boldsymbol{x}_i(t) N_i(\boldsymbol{x}), \tag{3.4}$$

where N_i is the total number of point. By using nodes and basis function, other physical quantities also can be written as

$$\boldsymbol{v} = \sum_{i=1}^{N_n} \boldsymbol{v}_i(t) N_i(\boldsymbol{x}). \tag{3.5}$$

Therefore, we can discritize the physical quantity $\boldsymbol{q}(\boldsymbol{x}, t)$ representing on the grid $\boldsymbol{q}_i(t)$ (denoted as i) by using grid node $\boldsymbol{x}_i$ and nodal basis function $N_i(\boldsymbol{x})$, and on the particle position $\boldsymbol{q}_p(t)$ (denoted as p) by using particle $\boldsymbol{x}_p(t)$ and delta function as basis function of particle.

Weak form

To apply the discrete formulation following standard Finite Element Method, we will obtain the weak form of momentum conservation equation. We prepare the vector valued

test function $\boldsymbol{w}(\boldsymbol{x},t)$, and multiplying Eq. (3.2) by test function $\boldsymbol{w}(\boldsymbol{x},t)$, integrating over the entire of material Ω,

$$\int_\Omega \rho \boldsymbol{w}(\boldsymbol{x},t)\cdot\frac{D\boldsymbol{v}}{Dt}d\boldsymbol{x}=\int_\Omega \rho \boldsymbol{w}(\boldsymbol{x},t)\cdot\nabla\cdot\sigma^s d\boldsymbol{x}+\int_\Omega \rho \boldsymbol{w}(\boldsymbol{x},t)\cdot\boldsymbol{b}d\boldsymbol{x}, \tag{3.6}$$

where σ^s is specific stress $\rho\sigma^s=\sigma$.

Integrating by part of the first item on the right-hand side, we obtain the weak form of momentum conservation equation,

$$\begin{aligned}\int_\Omega \rho \boldsymbol{w}(\boldsymbol{x},t)\cdot\frac{D\boldsymbol{v}}{Dt}d\boldsymbol{x}=&-\int_\Omega \rho\nabla\boldsymbol{w}(\boldsymbol{x},t):\sigma^s d\boldsymbol{x}+\int_{\partial\Omega}\boldsymbol{w}(\boldsymbol{x},t)\cdot(\sigma\cdot\boldsymbol{n})d\boldsymbol{s}\\&+\int_\Omega \rho\boldsymbol{w}(\boldsymbol{x},t)\cdot\boldsymbol{b}d\boldsymbol{x},\end{aligned} \tag{3.7}$$

where $\boldsymbol{n}$ is unit normal vector on boundary, $d\boldsymbol{x}$ is the differential volume elements, and $d\boldsymbol{s}$ is the differential surface elements. Note that it is assumed that test function is $\mathbf{0}$ on the boundary.

We will discritize the weak form on particle by substituting Eq. (3.3) into Eq. (3.7), following $\int_\Omega \boldsymbol{q}(\boldsymbol{x},t)\delta(\boldsymbol{x}-\boldsymbol{x}_p(t))d\boldsymbol{x}=\boldsymbol{q}(\boldsymbol{x}_p(t),t)$,

$$\begin{aligned}\sum_{p=1} m_p\boldsymbol{w}(\boldsymbol{x}_p(t),t)\cdot\frac{D\boldsymbol{v}(\boldsymbol{x}_p(t),t)}{Dt}=&-\sum_{p=1} m_p\nabla\boldsymbol{w}(\boldsymbol{x},t)|_{\boldsymbol{x}=\boldsymbol{x}_p}:\sigma^s(\boldsymbol{x}_p(t),t)\\&+\int_{\partial\Omega}\boldsymbol{w}(\boldsymbol{x},t)\cdot(\sigma\cdot\boldsymbol{n})d\boldsymbol{s}+\sum_{p=1} m_p\boldsymbol{w}(\boldsymbol{x}_p(t),t)\cdot\boldsymbol{b}.\end{aligned} \tag{3.8}$$

Substituting the physical quantities and test function represented by grid node, $\boldsymbol{v}=\sum_{i=1}^{N_n}\boldsymbol{v}_i(t)N_i(\boldsymbol{x}),\boldsymbol{w}=\sum_{i=1}^{N_n}\boldsymbol{w}_i(t)N_i(\boldsymbol{x}),\boldsymbol{b}=\sum_{i=1}^{N_n}\boldsymbol{b}_i(t)N_i(\boldsymbol{x})$. Eq. (3.8) at time t^n (a superscript of n denote a quantity at time t^n) can be written as

$$\sum_{i=1}\boldsymbol{w}_i^n\cdot\sum_{j=1} m_{i,j}^n\frac{D\boldsymbol{v}_j^n}{Dt}=-\sum_{i=1}\boldsymbol{w}_i^n\sum_{p=1} m_p\nabla N_i(\boldsymbol{x})|_{\boldsymbol{x}=\boldsymbol{x}_p}\cdot\sigma_p^{s,n} \tag{3.9}$$

$$+\sum_{i=1}\boldsymbol{w}_i\cdot\tau_i^n+\sum_{i=1}\boldsymbol{w}_i\cdot\boldsymbol{b}_{,i}^n, \tag{3.10}$$

where $m_{i,j}^n=\sum_{p_1} m_pN_i(\boldsymbol{x}_p^n)N_j(\boldsymbol{x}_p^n)$ is the mass matrix, $\sigma_p^{s,n}=\sigma^s(\boldsymbol{x}_p^n,t^n)$ is the specific stress at particle, $\tau_i^n=\int_{\partial\Omega}N_i(\boldsymbol{x})(\sigma(\boldsymbol{x},t^n)\cdot\boldsymbol{n})d\boldsymbol{s}$ is the discrete applied traction, $\boldsymbol{b}_i^n=\sum_{p=1} m_pN_i(\boldsymbol{x}_p)\boldsymbol{b}(\boldsymbol{x}_p^n,t^n)$ is the discretized specific external force.

The Eq. (3.9) should satisfies the any components of test function $\boldsymbol{w}_i^n$ at time t^n, thus this discretized weak form of momentum conservative equation reduced to

$$\sum_{j=1} m_{i,j}^n\frac{D\boldsymbol{v}_j^n}{Dt}=-\sum_{p=1} m_p\nabla N_i(\boldsymbol{x})|_{\boldsymbol{x}=\boldsymbol{x}_p}\cdot\sigma_p^{s,n}+\tau_i^n+\boldsymbol{b}_i^n. \tag{3.11}$$

This Eq. (3.11) can be considered as discritized equation of motion to update velocity at the grid node i. In practice (in order to avoid calculating a inverse of the mass matrix), instead of a mass matrix, we use a lumped mass matrix where each raw component is grouped into diagonal components,

$$m_i^k = \sum_{p=1} m_p N_i(\boldsymbol{x}_p^k), \tag{3.12}$$

and the Eq. (3.11) can be rewritten by lumped mass matrix as

$$m_i^n \frac{D\boldsymbol{v}_i^n}{Dt} = -\sum_{p=1} m_p \nabla N_i(\boldsymbol{x})|_{\boldsymbol{x}=\boldsymbol{x}_p} \cdot \sigma_p^{s,n} + \tau_i^n + \boldsymbol{b}_i^n. \tag{3.13}$$

The nodal velocity Lagrangian update denoted t^L (Fig. 3.1(3)) is

$$\boldsymbol{v}_i^L = \boldsymbol{v}_i^n - \frac{1}{m_i^n} \sum_{p=1} m_p \nabla N_i(\boldsymbol{x})|_{\boldsymbol{x}=\boldsymbol{x}_p} \cdot \sigma_p^{s,n} + \frac{\tau_i^n}{m_i^n} + \frac{\boldsymbol{b}_i^n}{m_i^n}. \tag{3.14}$$

Particle to Grid and Grid to Particle Transfer

We introduce the APIC data transfer scheme [44] to prevent the loss of information. As the Grid to Particle transfer (Fig. 3.1(4)), the nodal quantity such as velocity $\boldsymbol{v}_i^n$ transfer into the particle quantity $\boldsymbol{v}_p^n$ by using standard basis function $N_i(\boldsymbol{x})$,

$$\boldsymbol{v}_p^n = \sum_{i=1} \boldsymbol{v}_i^n N_i(\boldsymbol{x}_p). \tag{3.15}$$

On the other hand, as the Particle to Grid transfer by using lumped mass matrix,

$$\boldsymbol{v}_i^n = \frac{1}{m_i} \sum_{p=1} m_p (\boldsymbol{v}_p^n + \mathbf{C}_{\mathbf{p,i}}^{\mathbf{n}}) N_i(\boldsymbol{x}_p), \tag{3.16}$$

where $\mathbf{C}_{\mathbf{p,i}}^{\mathbf{n}} = \mathbf{B}_p^n (\mathbf{D}_p^n)^{-1} (\boldsymbol{x}_i - \boldsymbol{x}_p^n)$ is APIC correction term [44], each term is $\mathbf{D}_p^n = \sum_{i=1} N_i(\boldsymbol{x}_p^n)(\boldsymbol{x}_i - \boldsymbol{x}_p^n)(\boldsymbol{x}_i - \boldsymbol{x}_p^n)^T$, $\mathbf{B}_p^{n+1} = \sum_{i=1} N_i(\boldsymbol{x}_p^n) \boldsymbol{v}_i^L (\boldsymbol{x}_i - \boldsymbol{x}_p^n)$.

Constitutive model

We compute the stress term through the constitutive equation. We followed Yue et al. [102] to apply the Herschel–Bulkley fluid, reproducing the shear-dependent viscosity and yielding behavior. As a hyperelastic stored (or strain) energy density function $W = W_v(J) + W_s(\overline{\mathbf{b}}^e)$, $W_v(J)$ is the volumetric term, $W_s(\overline{\mathbf{b}}^e)$ is the shear term,

$$W_v(J) = \frac{1}{2}\kappa \left[\frac{1}{2}(J^2 - 1) - \ln J \right], \tag{3.17}$$

$$W_s(\overline{\mathbf{b}}^e) = \frac{1}{2}\mu(\mathrm{Tr}[\overline{\mathbf{b}}^e] - 3), \tag{3.18}$$

where κ and μ are the bulk and the shear modulus, $J = \det(\mathbf{F})$, and $\bar{\mathbf{b}}^e = \det(\mathbf{b}^e)^{-1/3}\mathbf{b}^e = J^{-2/3}\mathbf{b}^e$ is the volume preserving left-Cauchy Green tensor. We can obtain the Kirchhoff stress tensor from this hyperelastic energy density function,

$$\boldsymbol{\tau} = \frac{\partial W}{\partial \mathbf{F}^e}\mathbf{F}^{eT} = \frac{\kappa}{2}(J^2 - 1)\mathbf{I} + \mu\,\mathrm{dev}[\bar{\mathbf{b}}^e]. \tag{3.19}$$

In the Eq. (3.19), the right hand side of the first term is the volumetric part of response related to such as a pressure, and the second term is deviatric part of response related to such as shear stress. We have used $\mathrm{dev}[\mathbf{x}] = \mathbf{x} - \frac{\mathrm{Tr}[\mathbf{x}]}{3}\mathbf{I}$, and $\mathbf{I}$ denotes the 3×3 Identity tensor. The Kirchhoff tensor is related to the Cauchy stress via $\boldsymbol{\sigma} = \boldsymbol{\tau}/J$.

In order to introduce the shear plasticity, we use the von-Mises yield condition [83, 69] to define the limits of the elastic regime,

$$\Phi(s) = s - \sqrt{\frac{2}{3}}\sigma_{HY} \leq 0, \tag{3.20}$$

where $s = \|\mathbf{s}\|_F$ is the magnitude of shear part of the Kirchhoff stress tensor ($\|\cdot\|_F$ denotes the Frobenius norm) as $\mathbf{s} = \mathrm{dev}[\boldsymbol{\tau}] = \mu\,\mathrm{dev}[\bar{\mathbf{b}}^e]$, and σ_{HY} is a yield stress as the yield condition. This means that the material behaves elastic under the condition $\Phi(s) \leq 0$, and if exceed the $\Phi(s) > 0$, the part of the strain violating the von-Mises yield condition can be considered as a plastic strain.

The update of the elastic part of the left Cauchy-Green tensor is given by $\dot{\mathbf{b}}^e = \mathbf{L}\mathbf{b}^e + \mathbf{b}^e\mathbf{L}^T + \mathcal{L}_{\boldsymbol{v}}\mathbf{b}^e$, where $\mathbf{L} = \nabla\boldsymbol{v} = \dot{\mathbf{F}}\mathbf{F}^{-1}$ is the spatial velocity gradient and, the last part $\mathcal{L}_{\boldsymbol{v}}\mathbf{b}^e$ is the Lie derivative of $\mathbf{b}^e$ along the velocity field. $\mathbf{L}\mathbf{b}^e + \mathbf{b}^e\mathbf{L}^T$ corresponds to the change in the total strain due to the velocity field, and the Lie derivative corresponds to the change in the plastic strain considering the plastic part of deformation gradient, i.e., the plastic flow that can be considered fluid flow. The Lie derivative is given by $\mathcal{L}_{\boldsymbol{v}}\mathbf{b}^e = -\frac{2}{3}\,\mathrm{Tr}[\mathbf{b}^e]\dot{\gamma}\hat{\mathbf{s}}$ (see Simo and Hughes [83]). $\dot{\gamma}$ is the flow rate or a scalar strain rate, and $\hat{\mathbf{s}}$ is the flow direction ($\hat{\mathbf{s}} = \mathbf{s}/s$ its normalized form). This flow rule is objective and can be derived by applying the principle of maximum plastic dissipation to the stored energy function (3.17) and the yield condition (3.20) [82]. By rewriting the Herschel–Bulkley model as a function of the strain rate, we obtain the following rule for the flow rate:

$$\dot{\gamma}(s) = \max\left(0, \left(\frac{\Phi(s)}{\eta_H}\right)\right)^{1/n_H}. \tag{3.21}$$

The specific implementation of this flow-rule based strain update follows the return mapping algorithm presented in Yue et al. [102]. The strain, first, is updated as the elastic material, and if the shear stress exceeded, the strain will correct to satisfy the flow rule and von-Mises yield condition. The implicit strain update as the elastic material can be written as

$$\bar{\mathbf{b}}^{e,\mathrm{pre}} = \bar{\mathbf{f}}^{n+1}\bar{\mathbf{b}}^{e,n}\bar{\mathbf{f}}^{n+1\ T}, \tag{3.22}$$

where $\mathbf{f}^{n+1} = \mathbf{I} + \Delta t \nabla \mathbf{v}^n$. If the shear stress given by $\bar{\mathbf{b}}^{e,\mathrm{pre}}$ satisfied with the von-Mises yield condition, the plastic flow does not occur. In the case of the shear stress exceed, the strain will correct. As an implementation, in order to satisfy the yield conditions and flow rule, the corrected shear stress is given by the solution of the formula,

$$\eta_H^{1/n_H}(s^{k+1} - s^{\mathrm{pre}}) + 2\tilde{\mu}\Delta t \left(s^{\mathrm{pre}} - \sqrt{\frac{2}{3}}\sigma_{HY} \right)^{1/n_H} = 0, \tag{3.23}$$

where $\tilde{\mu} = \frac{1}{3}\mathrm{Tr}[\bar{\mathbf{b}}^{\mathrm{pre}}]$. If the $\eta_H = 0$ or $n_H = 1$, the corrected stress is given as

$$s^{n+1} = s^{\mathrm{pre}} - \left(\frac{s^{\mathrm{pre}} - \sqrt{\frac{2}{3}}\sigma_{HY}}{1 + \frac{\eta_H}{2\tilde{\mu}\Delta t}} \right). \tag{3.24}$$

We obtain the s^{n+1} and the strain update with corrected strain,

$$\bar{\mathbf{b}}^{n+1} = \frac{1}{\mu}\mathbf{s}^{n+1} + \frac{1}{3}\mathrm{Tr}[\bar{\mathbf{b}}^{\mathrm{pre}}]\mathbf{I}, \tag{3.25}$$

where $\mathbf{s}^{n+1} = s^{n+1}\hat{\mathbf{s}}^{\mathrm{pre}}$.

According to this implementation, The deformation gradient tensor $\mathbf{F}^n$ and the elastic part of the left Cauchy-Green tensor $\bar{\mathbf{b}}^{e,n}$ is updated to the $\mathbf{F}^L, \bar{\mathbf{b}}^{e,L}$ and the stress is computed on each particle.

Material Point Update

According to computing the stress and update the strain following the constitutive model and its implementation, we obtain the updated velocity at $\boldsymbol{v}_i^L$ the node and each strain tensor $\mathbf{F}_p^L, \bar{b}_p^{e,L}$. Each velocity at the particle position $\boldsymbol{x}_p^n$ corresponding to the updated particle velocity is interpolated by the nodal basis function,

$$\boldsymbol{v}_p^L = \boldsymbol{v}^L(\boldsymbol{x}_p^n) = \sum_{i=1} \boldsymbol{v}_i^L N_i(\boldsymbol{x}_p^n) \tag{3.26}$$

$$= \boldsymbol{v}_p^n + \Delta t \sum_{i=1} \frac{D\boldsymbol{v}_i^n}{Dt} N_i(\boldsymbol{x}_p^n). \tag{3.27}$$

During the velocity updated at Lagrangian step, the entire material will deform (Fig. 3.1(5)). According to the deformation of node grid at the Lagrangian step, the particle position is also moving due to the velocity at the $\mathbf{x}_p^n$ interpolating by the nodal basis function,

$$\boldsymbol{x}_p^L = \boldsymbol{x}_p^n + \Delta t \sum_{i=1} \boldsymbol{v}_i^L N_i(\boldsymbol{x}_p^n). \tag{3.28}$$

We obtain the updated material position and velocity at t^{n+1},

$$\boldsymbol{x}_p^{n+1} = \boldsymbol{x}_p^L, \tag{3.29}$$

$$\boldsymbol{v}_p^{n+1} = \boldsymbol{v}_p^L. \tag{3.30}$$

The strain property is also updated after the velocity update (Fig. 3.1(6)).

3.2 Fluid Measurement Methods

3.2.1 Over view of fluid measurement

In order to measure the fluid flowing property, we use the rheometer. A rotational rheometer is an appropriate method when measuring the unknown material flowing behavior first [59, 61]. The advantage of this method is that it can reproduce a Couette flow parallel to the direction of rotation. From the torque of the fixture and the rotation speed, the relation between shear stress and shear rate of the fluid can be determined. Each point of the flow curve can be measured directly by controlling the torque and rotation velocity. There are three main types of rotational rheometers: coaxial cylinder, cone-plate, and parallel-plate [59]. In this thesis, we used the cone-plate and parallel-plate rheometer introduced in Section 3.2.2.

The cone-plate rheometer is most suitable for measuring the flow curve of including non-Newtonian fluids because the shear stress and shear rate can be derived from the torque and rotational velocity without assuming a model of the flow curve. However, this rheometer have limitation to measure fluids that may contain small diameter particles, because the distribution of particles near the tip of the cone may become non-uniform and disturb the Couette flow. The parallel-plate can handle this limitation by adjusting the gap size but cannot reproduce uniform shear rate flow and assuming model. The Coaxial cylinder with a narrow gap is also suited for measuring non-Newtonian fluid, but the method does not apply to fluids containing large particles due to the narrow-gap limitation. This method can be scaled up to adapt to fluids containing large particles such as concrete [37]; note that assuming velocity distribution across the gap is linear with a narrow gap coaxial cylinder. In order to measure these complex fluids more accurate, Coussot et al. [11] use the large-scaled coaxial cylinder for natural coarse suspension. Flow fields of wide gap coaxial cylinder are analyzed to measure concrete [37], fabric-flow [58].

Other types of rheometers are also investigated [61]. A capillary rheometer measures the pressure exerted on the fluid flowing through the tube, assuming steady Hagen-Poiseuille flow, and obtains the relation of shear strain and shear stress, especially the high shear rate region. Ball-Falling is a measurement of the velocity of a sphere moving in a fluid under gravity, assuming the flow past a sphere. It is a simple setup and has been used for viscosity measurement.

It is not always necessary to obtain a flow curve or a viscosity to know the flowing property of a fluid. If we just want to compare the consistency of different fluids, there are simpler measurement methods applying for even complex fluids. Bostwick meter and Adams rheometer measure a length of spread from a certain initial shape by gravity. It can measure high viscous fluid containing some solid material such as tomato paste. A flow cup is a method that measures the time it takes for the fluid from a cup with a hole for fluid flowing out to compare and measure the consistency [61]. The

rotating vane rheometer has been used to measure the torque and rotational velocity corresponding flow resistance for the various complex fluids. Vane geometry can be adaptively chosen depending on the material to be measured [61]. From the results of these experimental devices, several methods have been investigated for obtaining the apparent viscosity of Bostwick measurement [62] or model parameter of the flow curve for Brookfield rheometer [98]. However, their accuracy depends on the measured material and is unclear [4, 63].

3.2.2 Cone- and Parallel-plate measurement

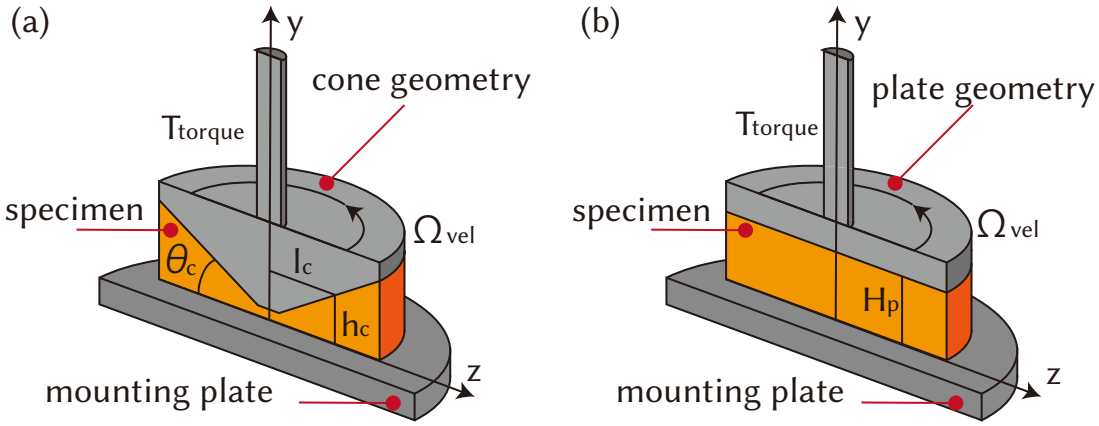

Figure 3.2: Illustrating the cone-plate (a) and parallel-plate rheometer (b).

In this thesis, we use a cone- and parallel-plate experimental device to measure the flow curve. We introduce the cone and parallel plate measurements [59].

In these measurement methods, as shown in Fig. 3.2, the fluid to be measured is sandwiched between the flat platform at the bottom pace and a cone or parallel plate instrument at the top, and cone or parallel plate rotates at a certain angular velocity Ω_{vel}. We measure the angular velocity Ω_{vel} and the torque T_{torque} generated at that time. The fluid is assumed to have the Couette flow along the direction of rotation of the cone- or parallel-plate, and from the hydrodynamic equations, the relationship between the shear rate $\dot{\gamma}$ and the shear stress σ_s is derived from the measured Ω_{vel} and T_{torque} [59].

For the cone-plate rheometry, we assume that θ_c is sufficiently small and stationary Couette flow occurring to the rotational direction. The rotational speed at the $r = l_c$ is $s_c = l_c\Omega_{vel}$. The height from mounting plate to cone geometry is $h_c = l_c \tan(\theta_c)$, and the rotational speed can be written as the $s_c = \frac{h_c\Omega_{vel}}{\tan(\theta_c)}$. Following to the Couette flow assuming (due to the θ_c is very thin; 0.5 or 1.0), the flow velocity towards the rotational direction is linear according to the height, the shear rate is $\dot{\gamma} = \frac{s_c}{h_c} = \frac{\Omega_{vel}}{\tan(\theta_c)}$ as constant form. For the parallel-plate rheomety, the height from the mounting plate to the plate geometry is constant H_p. Like the cone-plate rheometry, let consider the shear rate in this case. The rotational speed at the $r = l_p$ is $s_p = l_p\Omega_{vel}$, and the shear rate can be

written as the $\dot{\gamma} = \frac{s_p}{H_p} = \frac{l_p \Omega_{vel}}{H_p}$, which is not constant depending on the radial length l_p. Therefore, when we measure the unknown fluid, which may have highly shear dependent viscosity, we may first use the cone-plate rheometry [61, 59]. However, the cone-plate rheometry has a limitation for the fluid containing some particle inclusion because the inclusion may directory contact the geometry close to the edge region and disturb the steady Couette flow. The accuracy of the measured flow curve depends on the validity of the assumptions of the fluid flow field; in the rotational rheometer assuming Couette flow, the measured flow curve is less accurate if reproducing flow in measuring is depart from assumed Couette flow due to the influence of fluid complexity such as containing solid particle. Therefore, the appropriate device geometry settings (such as cylinder radius, gap size, cone angle) to produce the assumed flow have been investigated, and established [61], which is a limitation of methods.

3.2.3 Laboratory device and Herschel–Bulkley fitting

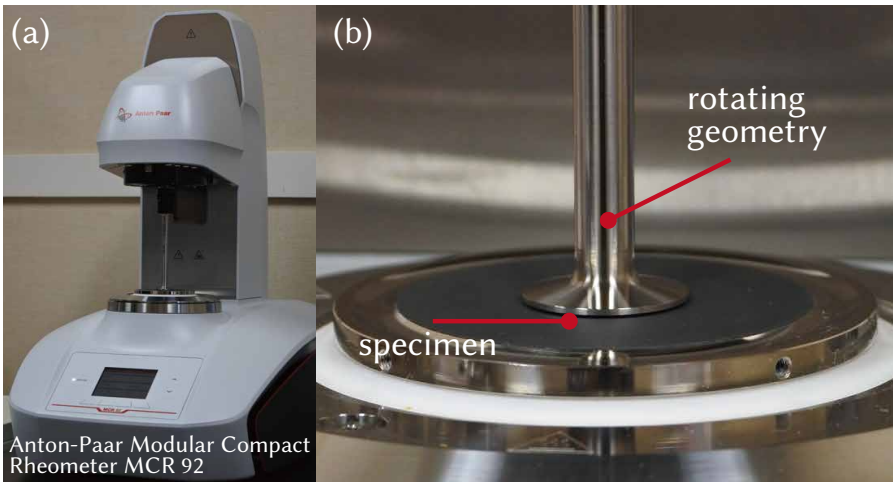

Figure 3.3: The rheometer device we use, (a) is the entire device, (b) is the rotating part and platform of the rheometer. This figure is the reuse of the published article [66].

We use a laboratory device, rheometer (Anton-Paar Modular Compact Rheometer MCR 92, Fig. 3.3) that can cone-plate and parallel-plate measurement by switching the geometry. We measured various fluid-like food as the available and common complex fluids containing widely class of flowing behavior. The measured data is dotted curves as shown in Fig. 3.4. We can see the various types of the dotted curve, and most of the curve is nonlinear. These linear and nonlinear flow curves can be fitted by the Herschel–Bulkley model given by $\sigma_s = \sigma_{HY} + \eta_H \dot{\gamma}^{n_H}$.

We employed the fitting by solving the following minimization problem per each

Sauce	n_H	η_H [Ba $\cdot s^{n_H}$]	σ_{HY} [Ba]	geometry	temperature
Ho	0.997	173.91	4.06×10^{-6}	Cone	19.27°C
My	0.442	305.23	708.13	Cone	19.0°C
Os	0.903	98.19	4.70×10^{-6}	Cone	18.39°C
Ke	0.524	34.04	271.86	Parallel	19.71°C
Hc	0.456	28.51	81.14	Parallel	19.22°C
Cm	0.782	70.89	10.27	Parallel	19.02°C
Ms	0.447	53.96	109.20	Parallel	19.18°C
To	0.518	37.51	37.43	Parallel	19.02°C
Sr	0.396	122.66	143.44	Parallel	18.3°C
Ch	0.809	59.56	28.39	Cone	18.63°C
Ti	0.629	172.15	349.87	Parallel	19.27°C
Oy	0.62	16.14	26.48	Parallel	18.8°C
Bb	0.48	92.85	165.57	Parallel	18.59°C
Wo	0.928	0.12	0.16	Parallel	19.02°C

Table 3.1: We show the fitted Herschel–Bulkley parameter in the Fig. 3.4, the unit form is (CGS), where Ba = 0.1Pa; **Ho** : honey of SEVEN & i PREMIUM, **My** : Mayonnaise of Kewpie, **Os** : Oligosaccharide syrup of SEVEN & i PREMIUM, **Ke** : Ketchup of KAGOME, **Hc** : Hot chilli sauce of GOLDEN MOUNTAIN, **Cm** : Sweetened condensed milk of Morinaga Milk, **Ms** : Mustard of S&B, **To** : Japanese pork cutlet sauce of Bull-Dog, **Sr** : Sriracha hot chilli sauce of Flying Goose Brand, **Ch** : Chocolate syrup of Morinaga, **Ti** : Sweat bean sauce of LEE KUM KEE, **Oy** : Oyster sauce of SEVEN & i PREMIUM , **Bb** : BBQ sauce of McDonald ' s Japan, **Wo** : Worcestershire sauce of Bull-Dog.

material:

$$(\sigma_{HY}, \eta_H, n_H) = \mathrm{argmin}_{\sigma'_{HY}, \eta'_H, n'_H} \sum_{i=1}^{N_{\mathrm{sample}}} \left\| \frac{\sigma'_{HY} + \eta'_H \tilde{\dot{\gamma}}_{,i}^{\,n'_H} - \tilde{\sigma}_{s,i}}{\tilde{\sigma}_{si}} \right\|^2, \tag{3.31}$$

where N_{sample} is the number of different strain rate samples in the measurements, $\tilde{\dot{\gamma}}_{,i}$ and $\tilde{\sigma_{s,i}}$ are the strain rate and stress of the i-th sample. Note that the error is measured in the relative sense, to account for the fact that both the strain rate and stress of our interest range several orders of magnitude; we want to have good fit for both high and low strain rate regimes. We show the material parameters obtained from our measurements and fitting in Table 3.1.

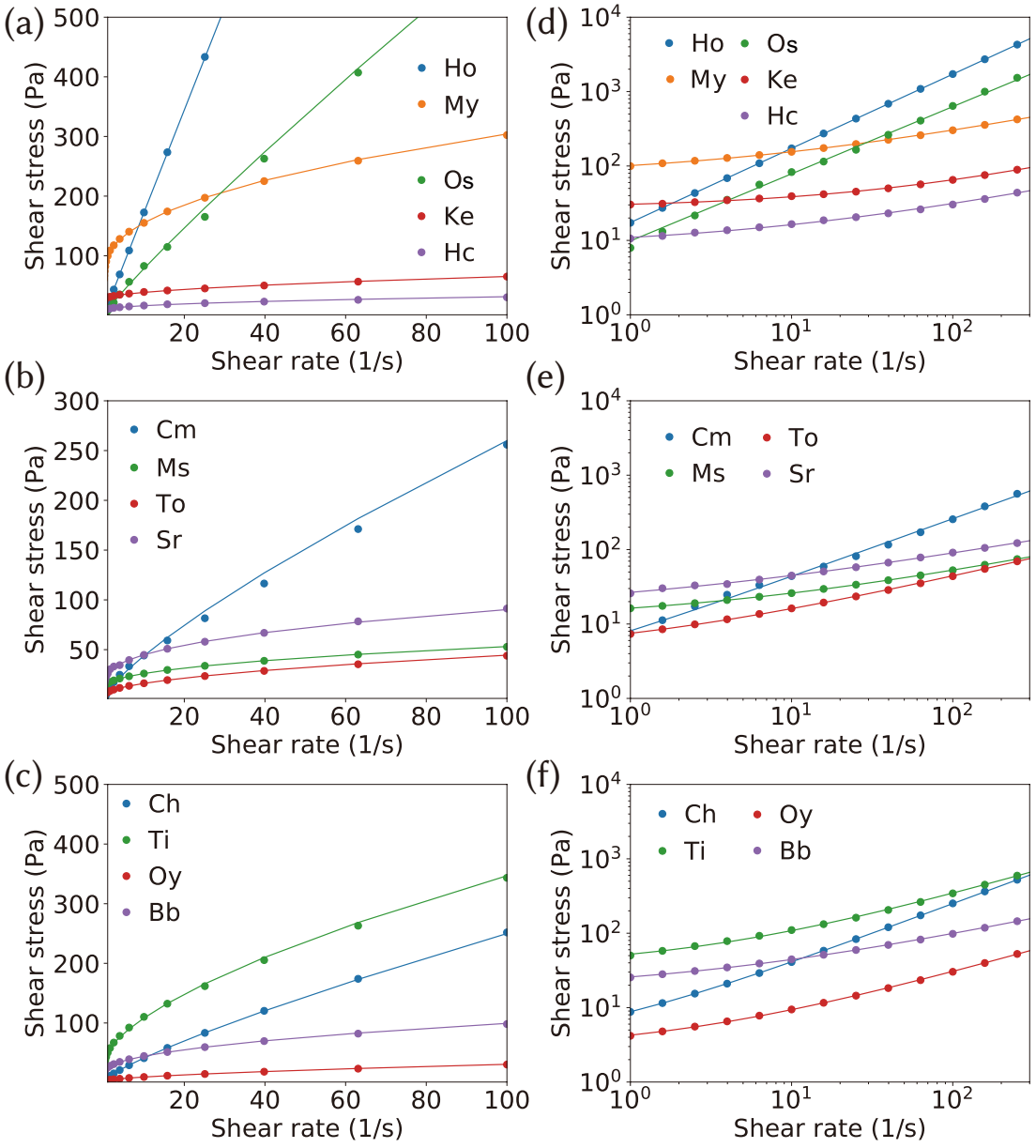

Figure 3.4: The measured data (dotted) listed on the Table 3.1 and fitting curve (solid line) of various fluid-like food as the available and common complex fluids containing widely class of flowing behavior. This figure is the reuse of the published article [66].

Chapter 4

Exploring the transition behavior related to the reproducing solid-like phenomena with exhaustive numerical simulation

This chapter is based on the publication: Classification of the reversible–irreversible transitions in particle trajectories across the jamming transition point, Soft Matter, Volume 15, Issue 38, August 2019 [65].

4.1 The density dependent RI transition behavior

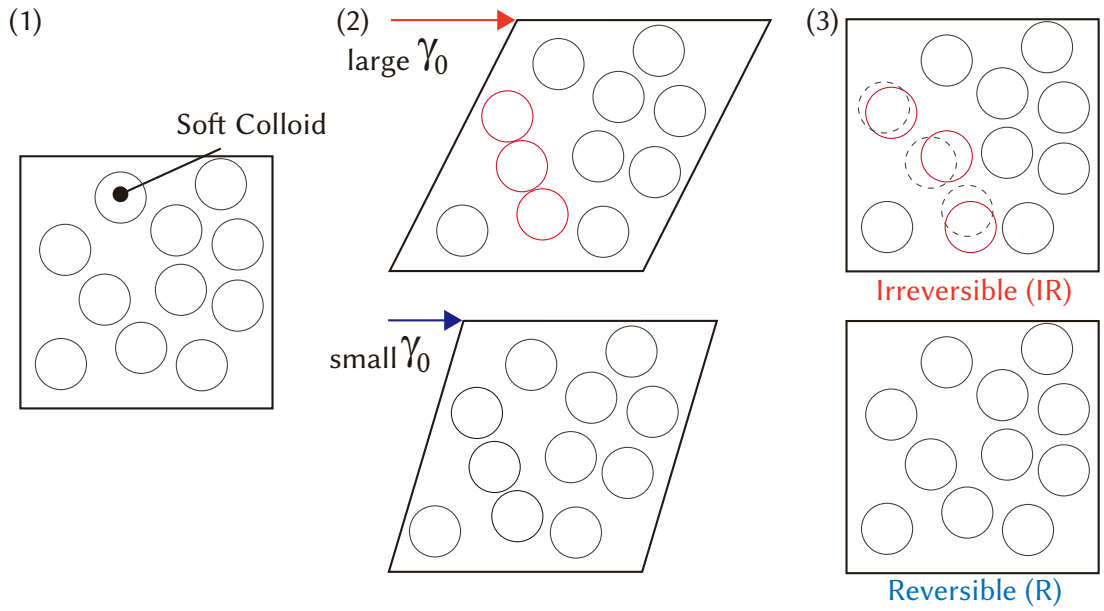

Figure 4.1: Illustrating the schematic picture of reversibility and irreversibility.

Some of the various complex fluids around us have solid-like properties, e.g., Mayo, toothpaste, shaving form. The jamming transition phenomenon is the key to understanding this solid-like behavior [92]. In order to approach the elastic property via jamming

phenomena, we focused on the athermal colloidal system as a disordered system of a complex fluid. As following jamming phenomena, the limit of reproducing the solid-like property depends on the density of colloidal suspension, especially crossing the jamming transition density φ_J, the physical property changing critically. As the low density under the φ_J, the system behaves as a fluid and flow. On the other hand, the high density over the φ_J, the system shows a solid-like behavior as a jammed system, which can resist the small shear stress with deforming reversibly, whereas applying the large shear stress, the system flow and the trajectory of the internal element are irreversible and diffusive.

As a phenomenon related to the qualitative change in physical properties across the φ_J, the reversibility of colloidal particles under the oscillatory shear and its behavior changes are known. Recently, studies have been focused on the microscopic reversibility of the constituent particles and their corresponding macroscopic behavior in colloidal dispersion systems under cyclic shear. The reversibility of particles in the fluid is related to the non-equilibrium phase transitions from the elastic amorphous phase to the plastic and flowing phase, and the reversibility depends on the particle density, especially jamming transition density. Fig. 4.1 shows the reversible and irreversible of oscillatory sheared colloidal system schematically. When the cyclic shear strain amplitude is small, each particle will return to its original position every one cycle (or several cycles), finding optimal trajectories (reversible trajectory) after sufficient oscillatory shear cycles. On the other hand, the amplitude exceeds a certain critical threshold; the particles will not return anymore because their trajectories are diffusive (irreversible trajectory). This transition is know to as the Reversible-Irreversible (RI) transition [39, 38].

This RI transition has been investigated mainly in two different density regimes, low and high density. Pine et al. and Corte et al. [72, 10] have shown that the RI transition occurs in a system of low-density colloidal suspensions. It was shown that when the shear strain amplitude exceeds a certain critical value, a continuous transition to irreversibility occurs due to the loss of reversibility caused by collisions between particles during periodic shear and hydrodynamic interactions that destabilize the particle trajectories during one cycle.

In the case of soft particles, it is known that particle trajectory can be reversible if the shear amplitude is smaller than a certain critical amplitude, even when the density is higher than the jamming transition density φ_J trajectories will be complexly colliding with several particles during a cycle. Interestingly, at the high densities region, the RI transition shows a discontinuous transition; when the shear amplitude exceeds the critical value, the number of particles taking irreversible trajectory takes on a discontinuous finite value [50, 46, 91].

Therefore, the RI transitions are qualitatively different since they are continuous and discontinuous transitions at low and high densities. This qualitative change is related to jamming and the limit of elastic properties; however, few cases have been investigated in the density region between high and low density. Thus this relation is also not clear.

Recently, Schreck et al. [80] have studied the RI transition in a wide range of densities below φ_J and strains. They defined the reversible phase as two separate phases; point-reversible phase and loop-reversible phase. In the point-reversible phase, the particles will find the particle configuration, which does not collide during the oscillatory cycles. In the loop-reversible phase, the trajectories of the particles are highly non-affine due to the colliding but reversibly come back to the original position after every (or several) cycle(s). On the other hand, the relationship between the rheological properties and the particle configurations slightly below φ_J is investigated by Vinutha et al. [93, 94], who found that the stationary configurations of the frictionless particles under quasistatic uniform shear are analogous to those of the shear-jammed frictional particles. These results suggest that the nature of the RI transition at the intermediate density region is very rich and can not be described as a mere extrapolation from the low-density region. Related results in three dimensions are presented [14].

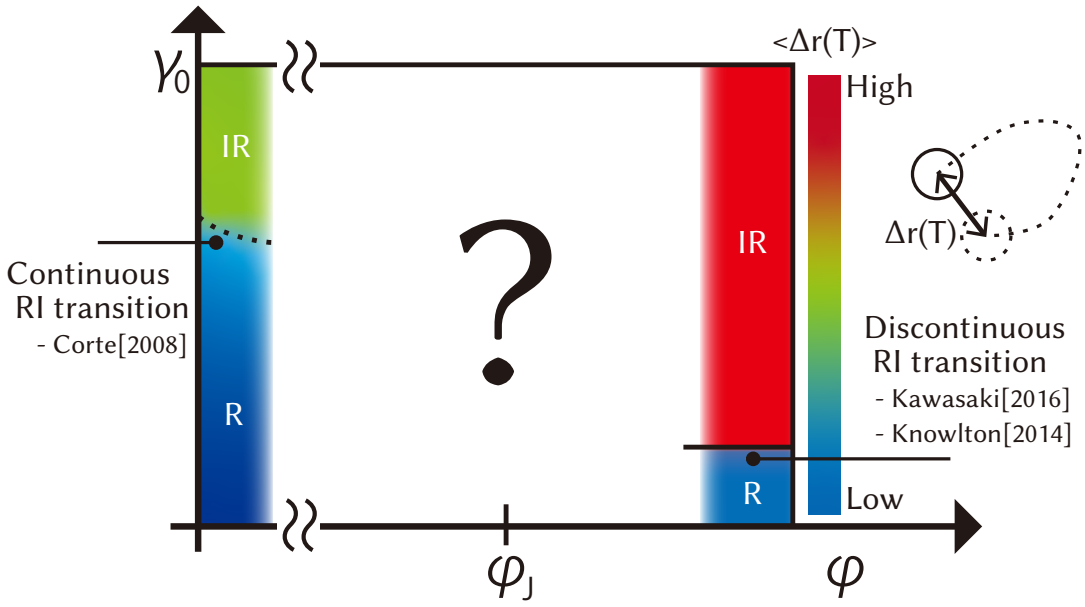

Figure 4.2: Illustrating the schematic picture for our purpose. RI transitions are known to be qualitatively different continuous and discontinuous transitions at low and high densities. These result illustrate schematic as color map $\Delta r(T)$ is the one-cycle displacement, and the color shows the amplitude of $\Delta r(T)$; blue is $\Delta r(T) \sim 0$, i.e., green and red is $\Delta r(T) > 0$,i.e., Reversible state (R). The RI transition behavior are investigated the low and high density limit, However the research of intermediate density region, especially around φ_J are a few. Therefore, we investigate the these intermediate region by using the exhaustive numerical simulation and grasp the big picture of transitions.

Fig. 4.2 shows the our purpose schematically. We investigate these RI transition behavior around φ_J by exhaustive numerical simulations with broad particle densities across the φ_J and shear strains, and we will make the phase diagram of RI transition to

grasp the big picture of transitions. Based on the phase diagram, we search for changes in mechanical properties and the presence of structures that characterize them.

4.2 Athermal soft colloidal suspension system

Athermal soft colloidal suspensions are modeled by a two-dimensional system of particles interacting with a harmonic mutual potential. The system is a equimolar binary mixture of frictionless particles with two different particle sizes (the size ratio is $\sigma_{\mathrm{L}} : \sigma_{\mathrm{S}} = 1.4 : 1$) to avoid the crystallization [92], and a jamming transition density $\varphi_{\mathrm{J}} = 0.842$ [57]. For this system, simulations of cyclic oscillatory shearing were performed with two different protocols. The particles are driven by the overdamped equations with Stokes' drag force with the finite-frequency oscillating shear protocol. The equation of motion is given by

$$\zeta_{\mathrm{s}} \left[\frac{\mathrm{d}\mathbf{r}_i}{\mathrm{d}t} - \dot{\gamma}(t) y_i(t) \mathbf{e}_x \right] + \sum_j \frac{\partial U(r_{ij})}{\partial \mathbf{r}_i} = 0, \tag{4.1}$$

$$U(r_{ij}) = \frac{\varepsilon}{2} \left(1 - r_{ij}/\sigma_{ij}\right)^2 \Theta(\sigma_{ij} - r_{ij}), \tag{4.2}$$

where ζ_{s} is a friction constant, $r_{ij} = |\mathbf{r}_i - \mathbf{r}_j|$ is the interparticle distance between the i-th and j-th particles, $\mathbf{e}_x = (1, 0)$ is the direction of the shear, and $\dot{\gamma}(t)$ is the shear rate. We use the interaction potential as $U(r_{ij})$, where ε is an energy scale, and $\sigma_{ij} = (\sigma_i + \sigma_j)/2$ is the interparticle distance at contact, $\Theta(x)$ is a Heaviside step function. We defined σ_{S}, $\tau_0 = \sigma_{\mathrm{S}}^2 \zeta_{\mathrm{s}} \varepsilon$, and each unit of length, time, energy, stress is ε^3.

An oscillatory deformation followed a Lees-Edwards periodic boundary condition, and the time evolution of shear stain is $\gamma(t) = \gamma_0[1 - \cos(\omega t)]$, where γ_0 is the amplitude of the imposed shear strain and $\omega = 2\pi/T$ is the oscillation frequency. In this finite shear protocol, The oscillation period T is mainly $T = 10^4 \tau_0$ choosing sufficiently large. We set an initial particle configuration as a random distribution at $t = 0$ and used the semi-implicit Euler's algorithm to solve Eq. (4.1). The time-step is $\Delta t = 0.1$; We have checked that using a higher-order discretization algorithm, such as the Heun method, does not change the results [1]. This is because the simulation is performed slowly enough with overdamped equations of motion to suppress the accumulation of rounding errors. Note that the velocity Verlet method used in micro-canonical molecular dynamics simulations is not applicable in our simulations because this system is fully overdamped. We use the system size of $L = 20$ in these results; we have checked that using a larger system size $L = 40$ does not qualitatively change the results. The maximal simulation time is $t_{\mathrm{sim}} = 4000T$. We perform at least five times independent simulations in each of the parameters sets (φ, γ_0) to improve the statistics; the bracketing symbol $\langle \cdots \rangle$ is used for describing an ensemble averages of variables discussed below.

4.3 Result and Discussion

4.3.1 Dynamics and phase diagram

The RI transition is characterized by the averaged particle displacements for one cycle $\Delta r(t, T)$.

$$\Delta r(t, T) = \frac{1}{N} \sum_{j=1}^{N} |\mathbf{r}_j(t + T) - \mathbf{r}_j(t)|. \tag{4.3}$$

This is a quantitative characterization of the reversibility of particle trajectories and is often used as an order parameter for RI transitions. If the system is in a reversible state, $\Delta r(t, T) \sim 0$, and in an irreversible state, it will take on a finite value. In this thesis, the system is considered to be in a reversible state when $\Delta r(t, T) < 10^{-6}$.

Dynamics of $\Delta r(t, T)$

As we discuss below, we have confirmed that when T is sufficiently large, the frequency dependence of $\Delta r(t, T)$ and phase diagram is small.

Fig. 4.3(a) shows the results for low densities $\varphi = 0.703$, far below φ_{J}. At $\gamma_0 \lesssim 0.40$, the displacement relaxes exponentially to zero. As γ_0 increases, the relaxation slows down and eventually reaches an irreversible state with finite $\Delta r(t, T)$'s following to a power-law tail (light blue line).

Fig. 4.3(b) shows the results for high densities $\varphi = 0.901$, far above φ_{J}. In this region, the relaxation behavior is qualitatively different from that of the low-density region. $\Delta r(t, T)$ takes a finite value (irreversivle state) in the beginning, but after a certain number of cycles, it discontinuously drops to zero entering a reversible state. It takes almost constant value until dropping down, insensitive to γ_0. $\Delta r(t, T)$ has a finite value at first, starting from the irreversible state with a finite value. However, the relaxation time in the irreversible state increases sharply with increasing γ_0 and eventually exceeds the time window of our simulation at $\gamma_0 \approx 0.14$. The previous study has shown that $\gamma_0 \approx 0.14$ where the relaxation time diverges matches with the yielding transition point γ_{Y} at which the system loses the elasticity and starts flowing [46]. Note that multi-period reversible; particles come back to their original positions only after several cycles (two or three), are observed at high densities region. In this thesis, we do not include multi-period data.

The results for intermediate densities between the low and high densities are surprisingly rich. Fig. 4.3(c) shows the results at $\varphi = 0.750$ below φ_{J}. If the γ_0 is small, the relaxation behavior of $\Delta r(t, T)$ is qualitatively the same as those at $\varphi = 0.703$ and it decays exponentially. As γ_0 increases, $\Delta r(t, T)$ starts developing the power-law tails. The relaxation time increases and eventually becomes larger than the simulation windows. As γ_0 increases further, however, this trend is reversed and the relaxation time becomes shorter. In other words, the system shows the reentrant behavior. After this reentrance such as $\gamma_0 = 0.30$, the relaxation behavior qualitatively changes and becomes

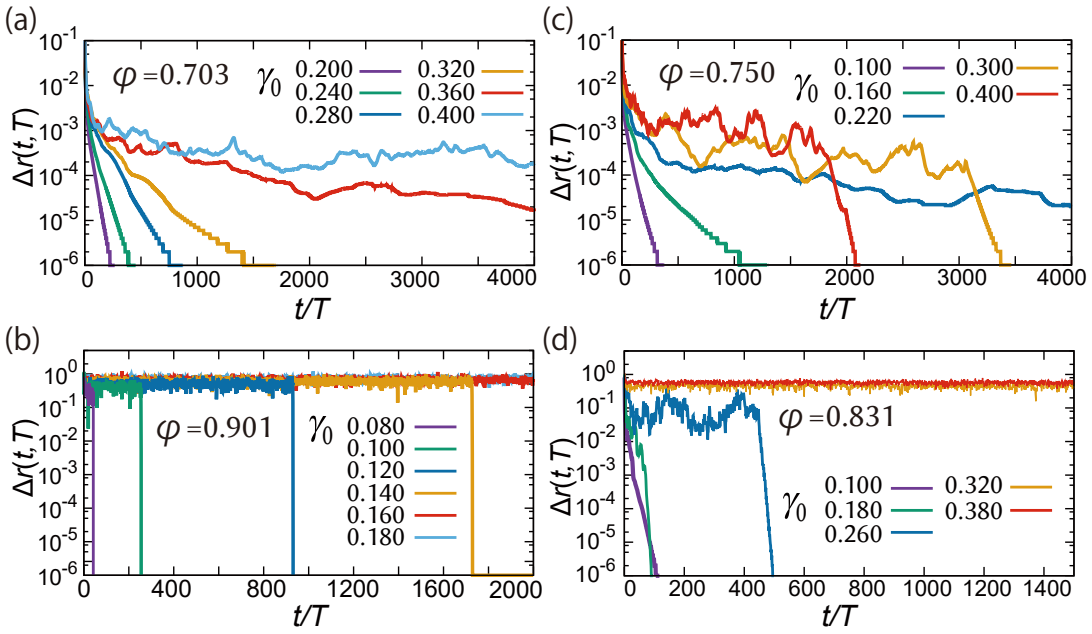

Figure 4.3: The time evolution of the averaged one-cycle displacement $\Delta r(t,T)$ in several densities from low to high density across the φ_J. We performed a single simulation for various strain amplitudes γ_0: (a) At $\varphi = 0.713$, far blow than the jamming transition density φ_J. For $\gamma_0 < 0.40$, the $\Delta r(t,T)$ continuously drops to zero. (b) At $\varphi = 0.713$, far above than the φ_J. For $\gamma_0 < 0.14$, the $\Delta r(t,T)$ discontinuously drops to zero. (c) At $\varphi = 0.750$, below the φ_J. For $\gamma_0 < 0.22$, the $\Delta r(t,T)$ continuously drops to zero. For $\gamma_0 \sim 0.22$ the $\Delta r(t,T)$ shows irreversible state for the full simulation time. For $\gamma_0 > 0.22$, we can observe that irreversible state reentrance to the reversible state, the $\Delta r(t,T)$ semi-discontinuously drops to zero. (d) At $\varphi = 0.831$, slightly below the φ_J, we can observe the transition, For $\gamma_0 < 0.30$, the $\Delta r(t,T)$ semi-discontinuously drops to zero. This figure is the reuse of the published article [65].

similar that observed above φ_J (Fig. 4.3(b)); it quickly decays to a plateau, stays there for a long time, and then abruptly and discontinuously drops to zero. Contrary to the results at $\varphi > \varphi_J$, the heights of the plateau increase continuously and the relaxation time shortens as γ_0 increases comparing $\gamma_0 = 0.30$ with $\gamma_0 = 0.40$. This reentrant transition of the relaxation time below φ_J is already reported by Schreck et al. [80]. We will analyze geometrical properties of these phases in the later section.

Fig. 4.3(d) is the result at $\varphi = 0.831$, slightly below φ_J. In this region, we again observe the exponential relaxation of $\Delta r(r,T)$ at very small γ_0, such as ($\gamma_0 = 0.1$). However, as γ_0 increases, the relaxation time barely increases and develops a plateau with finite height, whose behavior is more similar to what has been observed above φ_J (Fig. 4.3(a)), i.e., it decays rapidly to a plateau and then relaxes abruptly and step-wise to zero. For $\gamma_0 \gtrsim 0.3$, $\Delta r(t,T)$ remains constant in our simulation windows, suggesting that the system entered the irreversible state. It is interesting to observe a qualitatively

similar behavior to that above φ_J even in the unjammed phase. We will show that the RI transition observed in this density regime is closely related to the mechanical response (yielding) in the Section 4.3.2.

The phase diagram of IR

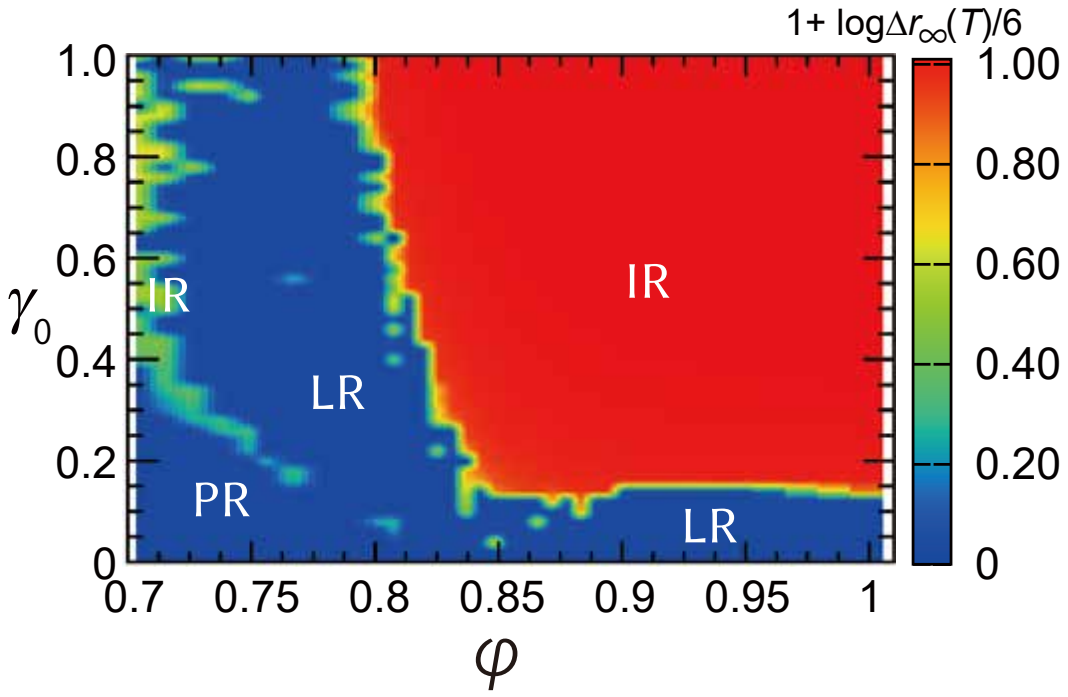

Figure 4.4: We show the phase diagram of RI transition on the parameter space of (φ, γ_0) by plotting the ensemble average of one-cycle displacement at the stationary state $\Delta r_\infty(T)$. In order to enhance the small values visibility, we used the $1 + \log \Delta r_\infty(T)/6$ as we define the color map. The blue region is the reversible state (PR means the point-reversible state, LR means the loop-reversible state) where the order parameter is $\Delta r_\infty(T) = 0$ (or more precisely $\Delta r_\infty(T) < 10^{-6}$). The green and red (please see the color column) region is the irreversible state (IR); especially the red means the largest value of $\Delta r_\infty(T) = 1$ (if the value $\Delta r_\infty(T) > 1$, clamp to $\Delta r_\infty(T) = 1$ for the visualization). This figure is the reuse of the published article [65].

We performed the simulation to obtain the $\Delta r(t, T)$ on the various parameter set of (φ, γ_0). As the order parameter of RI transition, we use the value of $\Delta r_\infty(T)$; we define the $\Delta r_\infty(T)$ is the ensemble average of $\Delta r(t = 4000T, T)$ judging the system reached the stationary state if becomes $\Delta r(t, T)$ independent of time. Note that the diffusion constant D is an alternative candidate of the order parameter. In Ref. [46], it is shown that the position of the RI transition is not affected by the choice of the order parameters if the period-doubling data are excluded.

The color map in Fig. 4.4 shows the phase diagram of RI transition from widely parameter space (φ, γ_0). In order to enhance the visibility of the small values, we used the $1 + \log \Delta r_\infty(T)/6$ as we defined the color map. We drew the blue as the reversible region where the order parameter is $\Delta r_\infty(T) = 0$ (or more precisely $\Delta r_\infty(T) < 10^{-6}$). We drew the green and red (please see the color column) as the irreversible region; especially the red means the largest value of $\Delta r_\infty(T) = 1$ (if the value $\Delta r_\infty(T) > 1$, clamp to $\Delta r_\infty(T) = 1$ for the visualization). In order to draw this figure, we simulated the system for the range of $0.7 \leq \varphi \leq 1.0$ and $0 \leq \gamma_0 \leq 1.0$ for grid points separated by $\delta\varphi = 0.05$ and $\delta\gamma_0 = 0.05$ for most cases. The finer grid sizes of $\delta\varphi = 0.01$ and $\delta\gamma_0 = 0.02$ are used in the vicinity of the phase boundaries. This phase diagram reflects the dynamic properties of $\Delta r(t, T)$ observed in Fig. 4.3.

We will look at this phase diagram in four density regions 1): $\varphi < 0.72$, 2): $0.72 \leq \varphi < 0.80$, 3): $0.80 \leq \varphi < 0.90$, 4): $0.9 < \varphi$. In 1): $\varphi < 0.72$, lowest density region, we observed the continuous RI transition from the point-reversible to the irreversible state, gradually changing from blue to green as γ_0 increases. It reflects the Fig. 4.3(a) of $\varphi = 0.703$ results.

In contrast 4): $0.9 < \varphi$, highest density region above the φ_{J}, we observe a discontinuous RI transition from the loop-reversible to the irreversible state, suddenly changing from blue to red as γ_0 increases. The transition phase boundary line is almost constant on the $\gamma_0 = 0.15$ over the all density φ_{J}. The abrupt change of the colors at $\gamma_0 = 0.15$ is a consequence of a sudden and discontinuous increase of $\Delta r_\infty(T)$ [46], it also reflects the Fig. 4.3(b) of $\varphi = 0.901$ results. The transition boundary is not exactly constant. As φ is decreased from above, it is slightly bent upward around $\varphi \approx 0.9$ and then downward as φ_{J} is approached, before it turns upward sharply at the edge at $\varphi = \varphi_{\mathrm{J}}$.

In 3): $0.80 \leq \varphi < 0.90$, the density region below the jamming transition density φ_{J}, the discontinuous transition from the loop-reversible to the irreversible state still presents, and its behavior will change interestingly. The transition boundary from blue to red rises upward sharply at $\varphi < \varphi_{\mathrm{J}}$. The presence of the discontinuous transition below φ_{J} is also observed in Ref. [80]. In the large γ_0 limit, this RI transition line seems to diverge at $\varphi \approx 0.8$. Note that this value is very close to the random loose packing density where the particles would undergo the mechanical transition if there is an interparticle frictional force. This result is reminiscent of the finding that configurations of the sheared frictionless spheres are similar to those of the shear jammed system of the frictional spheres reported in Ref. [93]. As for the values of $\Delta r_\infty(T)$ at $\varphi < \varphi_{\mathrm{J}}$, we will show the birds eye's view of $\Delta r_\infty(T)$ near φ_{J} in the Fig. 4.5. We can observe a discontinuity of the RI transition on both sides across the φ_{J}, but $\Delta r_\infty(T)$ tends to vanish at the $\varphi = \varphi_{\mathrm{J}}$, while the transition boundary is still unchanged. It is because the resolution of the parameters is too low and assessing the critical behavior of $\Delta r_\infty(T)$ at φ_{J} exactly is challenging due to a subtle interplay of the criticalities of the jamming and RI transitions [55, 12]. We shall revisit this issue in future work.

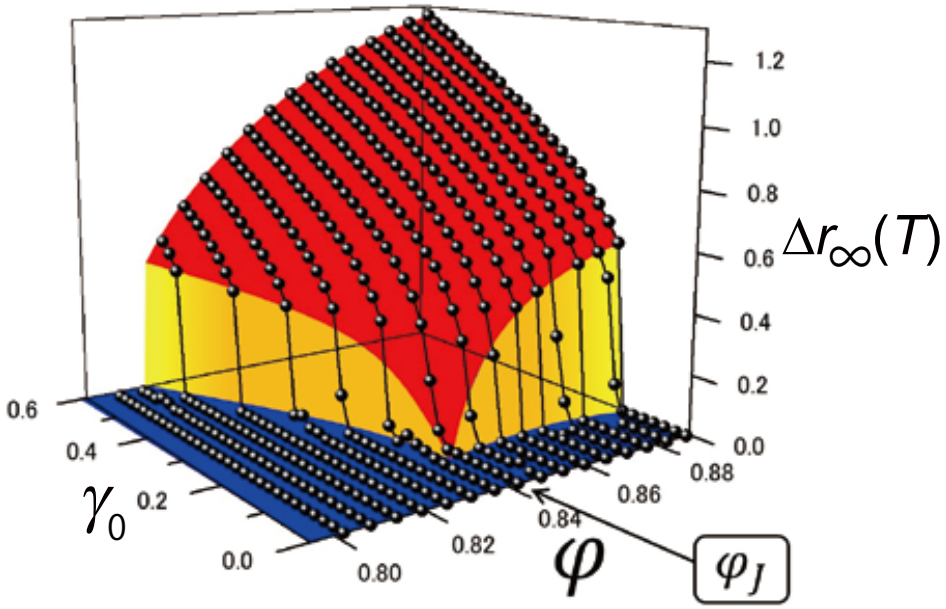

Figure 4.5: The bird's-eyes view of the phase diagram near φ_J plotting $\Delta r_\infty(T)$ as a function of φ and γ_0. We can observe the $\Delta r_\infty(T)$ discontinuously drops to zero at slightly below and above φ_J. This figure is the reuse of the published article [65].

In 2): $0.72 \leq \varphi < 0.80$, the low density region below φ_J, the behavior of the RI transition is also interesting. Most noticeably, there is a "peninsula" of the irreversible phase below φ_J (i.e., the green peninsula like region surrounded by the blue region), where $\Delta r_\infty(T)$ is finite (green) in the low density and small γ_0 region, surrounded by the reversible states (blue). It reflects the reentrant behavior as shown in Fig. 4.3(c). This region is surrounded by the two phase boundaries on the low γ_0 boundary side and upper boundary side. We found that the RI transition across the lower boundary side is continuous from the point-reversible to the irreversible state, whereas it is the discontinuous transition from the irreversible to the loop-reversible state at the upper boundary side. As the density increases, the upper and lower boundaries tend to converge to zero around φ_J. The phase boundaries of the irreversible phase, especially upper boundary, is jerky and blurred due to very large sample-to-sample fluctuations of $\Delta r_\infty(T)$. One may be tempted to consider this irreversible peninsula is a meta-stable state which vanishes in the large time limit ($t \to \infty$) or in the AQS limit ($T \to \infty$). However, this phase is unexpectedly stable and survives in the AQS limit simulation results [65].

Instead of the order parameter $\Delta r_\infty(T)$, one can employ the relevant time scales as the order parameters to draw the phase diagram. The phase boundaries are drawn as the points at which the time scales diverge. Note that there are two types of time scales in our systems depending on the nature of the RI transitions. If the transition is continuous, as we observe at low densities, $\Delta r_\infty(T)$ is well described by an exponential

function from which one can define the relaxation time τ_R. To define $\tau_{\rm R}$, we use an empirical function given by

$$\Delta r(t,T) = \Delta r_0 \frac{e^{-t/\tau_{\rm R}}}{t^{\delta}}, \tag{4.4}$$

where $\Delta r_0 \equiv \Delta r(t=0,T)$ [10]. On the other hand, if the transition is discontinuous, $\Delta r_\infty(T)$ develops a plateau. There are initial relaxations towards the plateau and the final abrupt drops from the plateau to the reversible phase. We refer to the time scale of the latter process as the life time $\tau_{\rm L}$ in order to discriminate the relaxation time $\tau_{\rm R}$ of the initial relaxation. The relaxation time $\tau_{\rm R}$ is obtained by fitting by the generalized expression of Eq. (4.4) given by

$$\Delta r(t,T) = (\Delta r_0 - \Delta r_{\rm s}) \frac{e^{-t/\tau_{\rm R}}}{t^{\delta}} + \Delta r_{\rm s}, \tag{4.5}$$

where $\Delta r_{\rm s}$ is the plateau value. On the other hand, we define the life time $\tau_{\rm L}$ as the time at which $\Delta r(\tau_{\rm L},T)$ drops to 10^{-6}.

The Fig. 4.6 (a) and (b) are the phase diagram as the color map of the averaged values of $\tau_{\rm L}$ and $\tau_{\rm R}$. The region above $\varphi_{\rm J}$ is not shown because it is identical to that for $\Delta r_\infty(T)$. In the vicinity of the phase boundary occurring the continuous RI transition, the iso-$\tau_{\rm L}$ line coincides with the iso-$\tau_{\rm R}$ line due to the continuous nature of the transition. On the other hand, near the reentrant transition, the two time scales are decoupled. While the region where $\tau_{\rm L} > 4000T$ (yellow colored region in Fig. 4.6 (a)) matches with the irreversible peninsula in the Fig. 4.4, The large $\tau_{\rm R}$ ridge only exists along the reentrant line as shown in Fig. 4.6 (b). These results support the existence of a peninsular region of the peninsula like irreversible phase and bolsters that the phase boundaries of the peninsula of the irreversible phase is delineated by the continuous transition at small γ_0's and discontinuous transition at large γ_0's. Schreck et al. [80] have demonstrated that this diverging time scale separates the reversible phase into the two distinct phases; the point-reversible phase where the one-cycle trajectory is completely affine-like and the loop-reversible phase where it is not. Our results suggest that there exist a (meta-)stable irreversible phase between the point- and loop-reversible phase.

4.3.2 The mechanical response depending of the density

The macroscopic mechanical responses, elasticity and plasticity, can be regarded as related to the reversibility or irreversibility of the system. The particle can take a reversible trajectory with respect to the displacement of the system, which corresponds to an elastic response. On the contrary, if the particle takes an irreversible trajectory and the particle trajectory diffuses, which corresponds to the occurring plastic flow in the system. The result of this is that the discontinuous RI transition line coincides with the yield transition line. We compute the shear stress σ_{xy} from the simulation of simple unidirectional shear with a constant strain rate $\dot{\gamma}$ given by

$$\sigma_{xy} = \frac{1}{2L^2} \sum_{j,k} \frac{x_{jk} y_{jk}}{r_{jk}^2} \frac{\partial U}{\partial r_{jk}}. \tag{4.6}$$

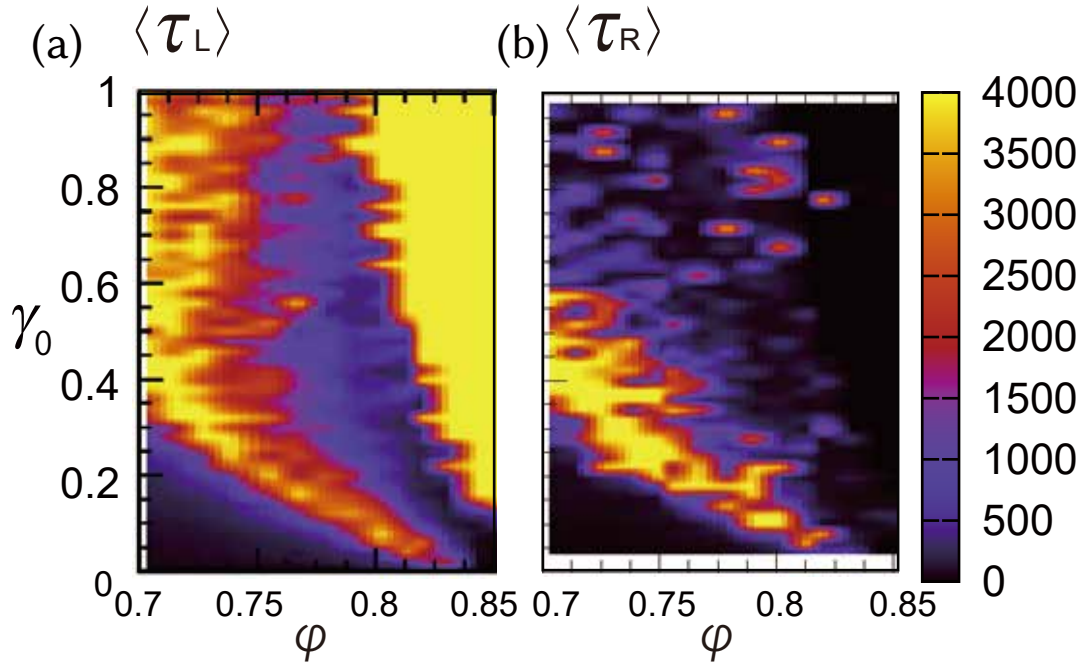

Figure 4.6: The color plot of (a) averaged lifetime of irreversible trajectories τ_{L} (the times $\Delta r(\tau_{\mathrm{L}}, T)$ drops to 10^{-6} and system become the reversible state), and (b) the averaged relaxation time τ_{R} defined by Eq. (4.5). The both color map clearly shows the existence of peninsula-like region. This figure is the reuse of the published article [65].

Fig. 4.7 is the strain (γ) dependence of σ_{xy} at $\dot{\gamma} = 10^{-5}$ for various φ below φ_{J} to verify the mechanical response. The stress-strain curves are averaged over 1000 independent initial configurations, which are generated by the AQS oscillatory shear simulations at $\gamma_0 = 1.0$ for each packing fraction. The stress-strain curve grows linearly. This indicates that the shear stress responds linearly to the displacement, corresponding to the elastic property of the system. When γ exceeds a certain value, it is the yielding transition point γ_{Y}, the stress-strain curve becomes a plateau and does not vary with displacement, indicating that the elastic property is lost and plastic flow is occurred due to the yielding transition. At each density below φ_{J}, the presence of elastic and plastic regimes has been confirmed. Interestingly, the yielding transition point γ_{Y} increases when φ decreases, and it matches with the discontinuous transition line as shown in Fig. 4.8 of white dots. This behavior is very similar to that observed experimentally in athermal colloidal suspensions below the glass transition point [60]. We can observe the more rich property in the elastic regime in the small strain region. Following the log-log plot of that stress-strain curve in Fig. 4.7(b), the curve is not linear against the elastic response, fitted by $\sigma \propto \gamma_e^a$. The nonlinear region can be divided into two regions by the fitting parameters: $a_e = 0.5$ and $a_e = 1.3$. For the $a_e = 0.5$, this is reminiscent of the softening of stress observed above φ_{J}. For the $a_e = 1.3$, This is again analogous with

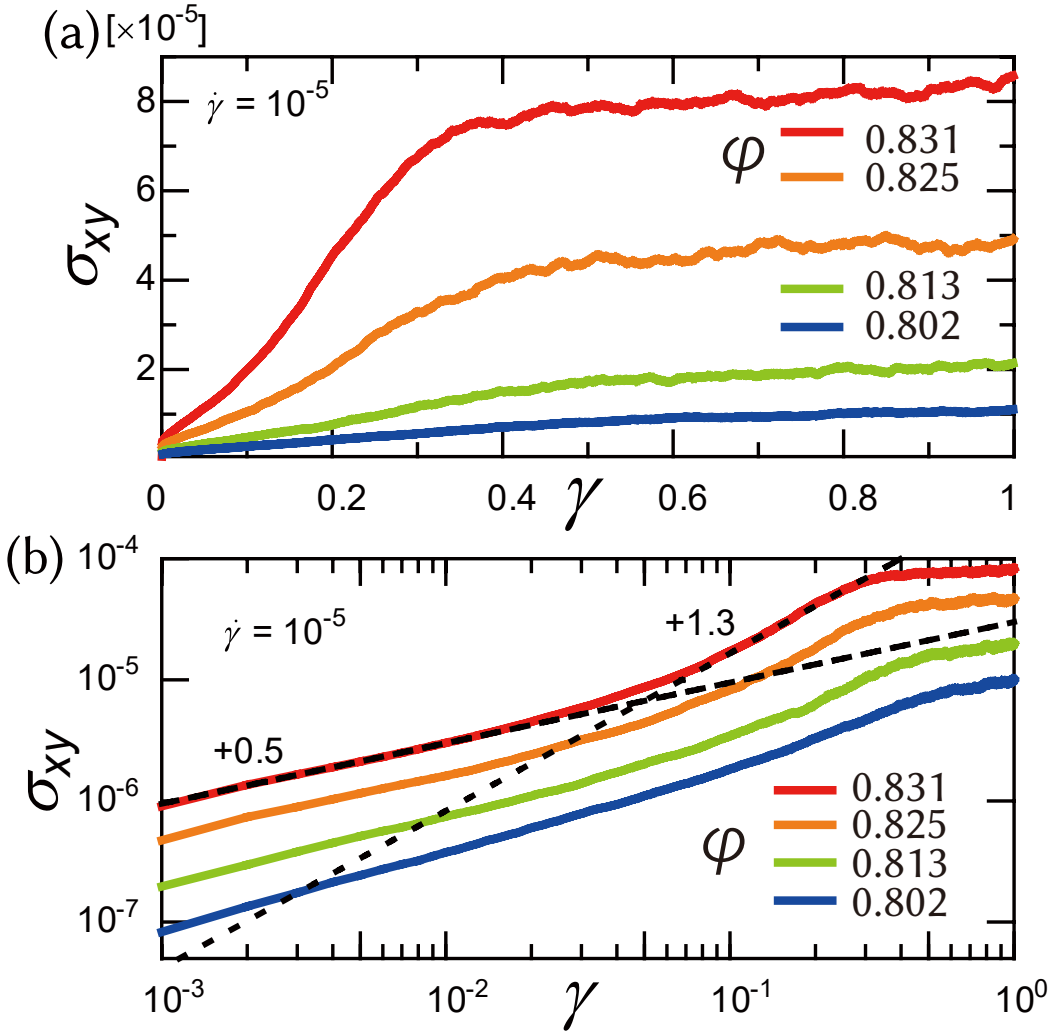

Figure 4.7: (a) is the stress-strain curves of near φ_J from the simulation of simple unidirectional shear with a finite constant strain rate $\dot{\gamma} = 10^{-5}$. The region where the σ_{xy} grows linearly shows elastic behavior, and the region where the σ_{xy} is constant shows yielding. we can observe the elastic and yielding behavior even in the below φ_J (b) is the same as the (a) but at small γ's in the log-log plot. we can observe the nonlinear elastic region where the shear stress is proportional to the $\gamma^{0.5}$ and $\gamma^{1.3}$. This figure is the reuse of the published article [65].

the findings reported above φ_J.

4.3.3 The relation between RI transition, mechanical property, and mesoscopical structure

The reversibility or irreversibility of a system is qualitatively determined as a result of the contact or collision of the respective particles. How collisions and contacts occur

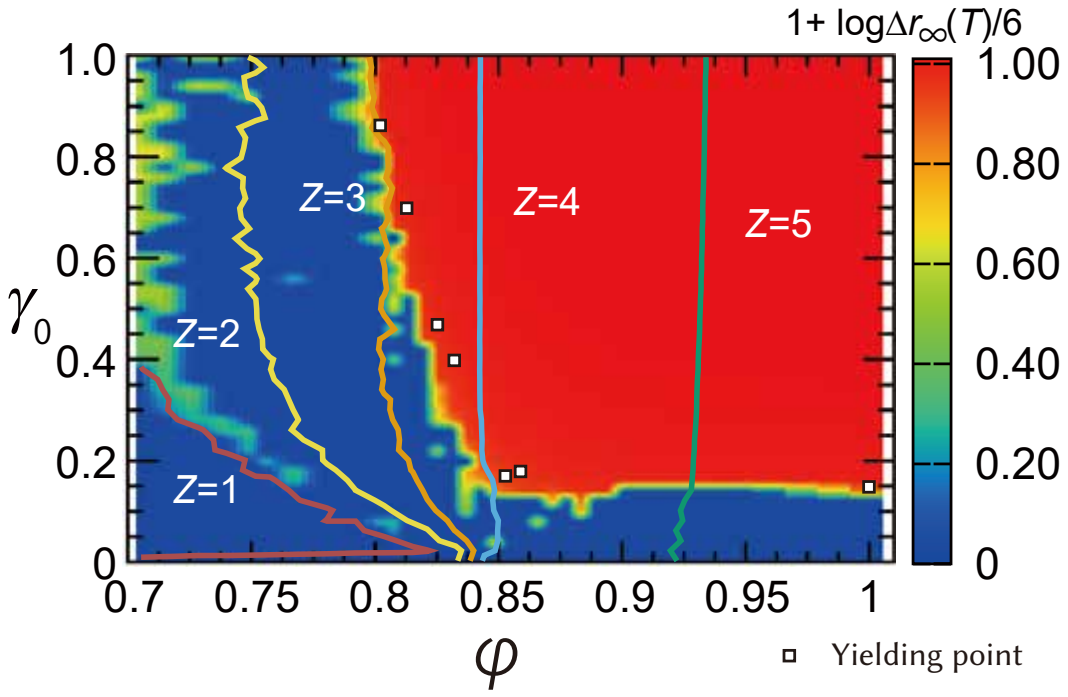

Figure 4.8: The iso-Z lines superimposed on the phase diagram shown in Fig. 4.4, square dots are the point that we observed yielding transition from steady shear simulation given by Fig. 4.7. The $Z = 0$ line agree with the continuous RI transition line from point reversible to irreversible. The $Z = 1$ line almost agree with the reentrant RI transition line from irreversible to loop reversible. The $Z = 3$, which the contact number related to the $Z = d + 1$ can make the system stabilize if the particle have the friction force, agree with the discontinuous RI transition slightly below φ_J. we plotted the yielding point as the white dot on the phase diagram given by the stress-strain curve. Some parts of this diagram are reused from published articles [65].

depends on the configuration of the particles reflecting the density and sheared state. In order to characterize the particles configurations related to the mesoscopic structure, we introduce the contact number Z of respective adjacent particles, which is known as the characterize the Jamming phenomena [92, 20]. A contact between particle i-th and j-th is defined when the particle distance r_{ij} is smaller than the $a_{ij} \equiv (\sigma_i + \sigma_j)/2$. We compute the Z_i counting the number of contact particles to $i-$th particle as satisfying the $r_{ij} \leq a_{ij}$, and we obtain the Z by averaging Z_i over the total particle.

Fig. 4.8 shows the iso-Z lines on the phase diagram. We have confirmed that the RI transition can be characterized by the contact number Z. We observed the $Z = 4$ line (light blue solid line) is vertically on the $\varphi \sim \varphi_J$ density line. It is expected the Maxwell's stability criterion [92], $Z = 4 = 2d$, where d is the number of the dimension. It also corresponds to the contact number occurring in the jamming transition with frictionless particles. The $Z = 5$ line is also a vertical line and on the higher density region from

φ_J. For $Z = 1$ to $Z = 3$, these iso-Z lines behave differently. They tend to converge towards below φ_J as γ_0 goes to 0, and are not parallel. Interestingly, we can observe that the $Z = 3$ line (orange solid line) corresponds to the discontinuous RI transition line by color changing from blue to red below φ_J density region. The contact number $Z = d+1$, is known as the specific contact number on the sheared particle system. As γ_0 increase, $Z = 3$ lines reaches $\varphi \approx 0.80$, which are known to be the random loose packing density. The $Z = 1$ line matches the continuous RI transition from point-reversible state to irreversible state, this implies that the first contact happened in oscillatory shear, and the system became irreversible.

4.4 Summary and conclusions

We have observed very rich phases and mechanical behaviors investigating the RI transition over a wide range density, especially below the φ_J, and also show that it can be characterized by the contact number.

In the low density region much below φ_J, there is a continuous transition from the point-reversible phase to the irreversible phase when γ_0 is increased at a fixed density. In the density region slightly larger than that density, as γ_0 is increasing, we observed a continuous transition from point-reversible to irreversible, and discontinuous transition from irreversible to loop-reversible occurs, irreversible phase is spread like a peninsula from around φ_J. Interestingly, the discontinuous phase transition from loop-reversible to irreversible is observed in not only high density region but also slightly below φ_J. In the slightly below φ_J, The system is completely stress-free in the AQS limit and thus the yielding transition is absent. However, the mechanical properties are encoded in the sheared particles configurations even below φ_J, we observed finite shear stress and the yielding behaviors as the strain rate $\dot{\gamma}$ increase in the simple shear situation. The yielding transition and RI transition points almost correspond even below φ_J. In addition, we found the nonlinear elastic response, at the small strains, proportional to $\gamma^{0.5}$ and $\gamma^{1.3}$. This implies the jamming criticality which controls mechanical and rheological behaviors near φ_J survive below φ_J.

The macroscopic behavior of the system, the reversibility and mechanical property, is the result of the sheared particles configuration and structure. The contact number Z can explain these behaviors nicely; several iso-Z lines correspond to the RI transition lines. The $Z = 1$ line related to the occurring first contact correspond to the continuous RI transition from point-reversible to irreversible state. The $Z = 3 = d + 1$, which the contact number can make the system stabilize if the particles have friction, agrees with the discontinuous RI transition slightly below φ_J.

It is well known that mechanical properties change as the particle density becomes φ_J, and the system obtains the solid-like behavior above φ_J. However, in these results from the quite simple model (frictionless and athermal colloidal model) by performing the exhaustive numerical simulation, qualitative changes of RI transition related to elasticity

and plasticity due to the jamming were observed even when densities are below φ_J under the shear conditions. It indicates that the phenomena caused by the density of particle inclusion in the complex fluid are more diverse around the φ_J. In addition, we observe that the RI transition corresponds to the yielding transition and the contact number reflected the mechanical property and the internal structure. It implies the possibility of characterizing and controlling these behaviors by using the contact number reflecting the particle configuration.

Chapter 5

Building a model to reproduce the nonlinear viscosity of mixtures with a data-driven approach

This chapter is based on the publication: Mixing Sauces: A Viscosity Blending Model for Shear Thinning Fluids, ACM Transactions on Graphics, Volume 38, Issue 4, July 2019 [66].

5.1 Mixture fluid behavior and representation

Figure 5.1: The pure honey (left), the pure mayo (right), the half-half mixture of them (middle). Both pure materials flow slowly and show stagnant behavior. However, the mixture looks flowing smoothly and has less viscous. Our motivation is to reproduce the material property of various mixtures, including the unintuitive behavior, from pure material property and mixing ratio. This figure is the reuse of the published article [66].

We focus on nonlinearly changing the viscosity in the mixing as an appreciative part of reproducing the complex fluids. The complex fluid viscosity is nonlinear (shear dependent), but also the viscosity changing behavior in the mixing is also nonlinear. The materials around us usually exist as a mixture of different constituents. For example, in cooking, we mix various fluid-like foods to make sauces, e.g., with the combination of ketchup and mayo, we can make aurora sauce. Each of the constituents of such

a mixture can be Newtonian or nonlinear viscosity. In Fig. 5.1, we show a captured footage of extruding the pure material and half-half mixture from the nozzle to the slope. The pure materials, honey, and mayo look high viscous and stagnant behavior. In contrast, the mixture exhibits a profoundly less viscous flow behavior compared to each fluid's edge. As the mixing ratio varies, the mixed material exhibits nonlinear viscosity changing and shows intriguing and nonintuitive behaviors.

In this chapter, the question is whether there is a way to describe and reproduce the material properties of such mixtures, not only for a particular combination but for a broader class of materials. This question looks difficult from the microscopic perspective because the internal elements of various complex fluids have various disorder systems, and their mixture is also quite disordered or unknown anymore. Therefore, we treat this question from the macroscopic perspective, and these fluids and mixtures are considered a homogeneous, which material property can be characterized by the flow curve. Because of the availability and the accuracy in the measurements of the materials, we limit the scope of our target to shear-thinning fluids of fluid-like foods, and we assume the thermostatic cases without chemical reactions. We seek the way of describing and reproducing of the blended material behavior as a change of flow curve.

A possible approach representing the mixing is to perform an exhaustive measuring and to have a database for all possible material mixtures. However, this approach would result in a combinatorial explosion of measurements. We thus pursue the viscosity blending model for describing the blended material property with the property of each pure constituent and their mixing ratios as the input. By using this approach, the measuring we need is only pure materials, and we can handle the mixture at the continuous mixing ratio.

5.1.1 Empirical viscosity blending in Newtoninan fluids

There are several known blending models to describe the viscosity of Newtonian fluids or the effective viscosity of Non-Newtonian fluids that have nonlinear viscosity at specific shear rate $\dot{\gamma}_s$ for mixing, all of which take the form of (5.25); $F(\eta) = \alpha F(\eta_A) + (1 - \alpha)F(\eta_B)$.

The linear blending is the most simple equation, $F(x) = x$:

$$\eta = \alpha\eta_A + (1 - \alpha)\eta_B. \tag{5.1}$$

The Arrhenius equation [3] is a multiplicative blending model with the choice of $F(x) = \ln(x)$:

$$\ln \eta = \alpha \ln \eta_A + (1 - \alpha) \ln \eta_B, \tag{5.2}$$

it can be written as $\eta = \eta_A^{\alpha}\eta_B^{1-\alpha}$. With the reciprocal function $F(x) = 1/x$, we recover the Bingham equation [45, 7]:

$$\eta^{-1} = \alpha\eta_A^{-1} + (1 - \alpha)\eta_B^{-1}, \tag{5.3}$$

with the choice of the one-thirds power, $F(x) = x^{1/3}$, we recover the Kendall and Monroe model [47]:

$$\eta^{1/3} = \alpha\eta_A^{1/3} + (1-\alpha)\eta_B^{1/3}, \tag{5.4}$$

and with the choice of $F(x) = 14.534\ln(\ln(x+0.8)) + 10.975$, we recover the Refutas method [2]:

$$\eta = \exp\left(\exp\left(\frac{\alpha\tilde{\eta}_A + (1-\alpha)\tilde{\eta}_B - 10.975}{14.534}\right)\right) - 0.8, \tag{5.5}$$

where $\tilde{\eta}_* = 14.534\ln(\ln(\eta_* + 0.8)) + 10.975$ for $* = A, B$. We note that the Refutas equation can be well approximated by $\eta^{-0.384} = \alpha\eta_A^{-0.384} + (1-\alpha)\eta_B^{-0.384}$ with a relative error less than 0.7%.

The calculated viscosity of an intermediate mixing ratio $0 < \alpha < 1$ satisfies $\eta = \eta_A = \eta_B$ when they have the same viscosity $\eta_A = \eta_B$, irrespective of the choice of α. And for $\eta_A \neq \eta_B$, a sublinear property $\eta < \alpha\eta_A + (1-\alpha)\eta_B$ (i.e., smaller than the linear estimate), as can be seen from the inset.

There is an outside of the class of the blending form $F(\eta) = \alpha F(\eta_A) + (1-\alpha)F(\eta_B)$, we will show the Lederer and Roegiers' model [56, 77] as for its example given by

$$\ln\eta = \frac{x_A}{x_A + \beta x_B}\ln\eta_A + \frac{\beta x_B}{x_A + \beta x_B}\ln\eta_B, \tag{5.6}$$

where x_A and x_B are the volume fractions of the materials A and B, respectively, and β is an empirical parameter. Because the mixing ratio α is related to x_A and x_B via

$$\alpha = \frac{x_A}{x_A + x_B} = \frac{1}{1 + x_B/x_A}, \tag{5.7}$$

Using this α, Eq. (5.6) can be rewrite as

$$\ln\eta = \frac{\alpha}{\alpha + \beta(1-\alpha)}\ln\eta_A + \left(1 - \frac{\alpha}{\alpha + \beta(1-\alpha)}\right)\ln\eta_B. \tag{5.8}$$

Writing $H(\alpha;\beta) = \frac{\alpha}{\alpha+\beta(1-\alpha)}$, we see that the Lederer and Roegiers' model belongs to the following class:

$$F(\eta) = H(\alpha;\beta)F(\eta_A) + (1 - H(\alpha;\beta))F(\eta_B), \tag{5.9}$$

which is a generalized version of (5.25). Now the question is whether the empirical parameter β in (5.9) can be chosen independently from the pair of materials A and B. If not, this means the model needs to be tuned per each combination, which could be hard to design.

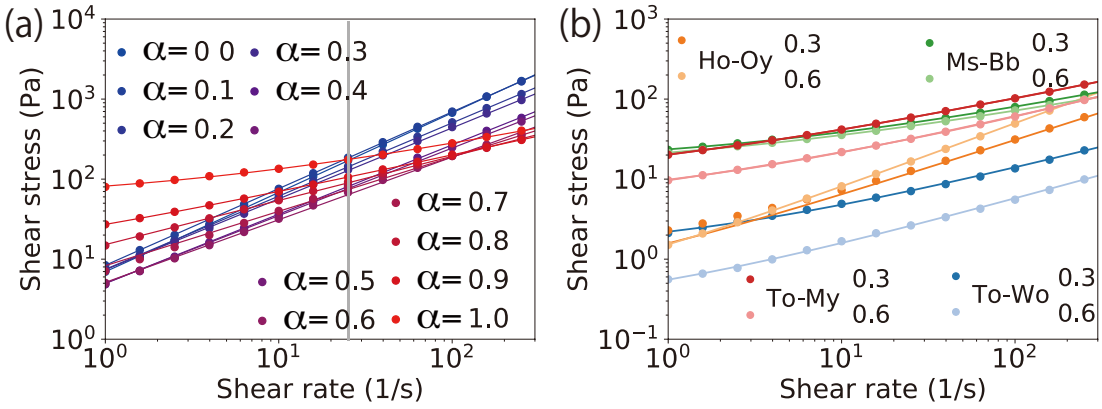

Figure 5.2: The measured flow curves of mixture in (a) and (b). Dots are measured data and solid lines are fitted line. We can observe the solid lines fitted to the Herschel–Bulkley model can nicely agree with the measured data of mixture. (a) Flow curve of the mixtures of honey (Ho) and mayo (My) with various mixing ratios $\alpha = 0.0,\ 0.1, 0.2, ..., 1.0$ (each color from blue to red corresponds to the each α). The gray vertical line shows the shear rate ($22s^{-1}$) at the intersection of the flow curves of pure mayo and honey. We can observe the effective viscosity of the mixture is lower than that of the pure one by looking at the shear stress on the gray line. (b) Flow curves for various combinations of mixtures. This figure is the reuse of the published article [66].

5.2 Flow curve behavior of mixture materials

Following the Section 2.1, the fluid flowing behavior can represent the relation between the shear stress and shear rate, i.e., flow curve. Now we consider how changes the flowing behavior of the mixture of fluids, which have linear or nonlinear viscosity as a changing of flow curve. We use the rheometer (Anton-Paar Modular Compact Rheometer MCR 92, see the Section 3.2.3) to measure the flow curves.

We measured the flow curve for mixed materials in Fig. 5.2. The Fig. 5.2(a) shows the results of mixtures of honey and mayo with various mixing ratios and those fitted to the Herschel–Bulkley model, Upon the measurements, we prepared the substances by stewing each of them with a fixed amount of time (40 times), for not only the mixtures but also the pure materials.

An interesting point of the flow curves of the mixture is that the shear stresses of the mixtures of various mixing ratios are smaller than those of the pure materials at the shear rate of 22s^{-1} (the gray line in Fig. 5.2(a)), where the shear stresses of the pure materials coincide. In other words, the effective viscosities of the two pure materials coincide at the point, but those of their mixtures are lower. The reduction in the viscosity in this example is almost an order of magnitude, and it cannot be ignored (as we demonstrated at the nozzle experiment in Fig. 5.1). We also performed measurements several times, and the flow curves were more or less the same.

Several conventional viscosity blending models [3, 45, 7, 47, 2] introduced previous section are known. As we described later at the Section 5.1.1, those models have the general blending form (5.25) : $F(\eta) = \alpha F(\eta_A) + (1-\alpha)F(\eta_B)$, where α is the mixing ratio, η_A and η_B are the viscosities of the two constituents, and F is an invertible function that depends on the model. All of these models fail to reproduce the characteristic behavior of the mixture, which is a decrease in the effective viscosity. Because if the viscosity are same as $\eta_A = \eta_B$, their predictions all provide $\eta = \eta_A = \eta_B$, irrespective of the choice of α and F. Therefore, we are faced with the fact that a mixing model that only considers the effective viscosity and mixing ratio cannot reproduce the characteristic behavior observed in plots and in real footage. This point implies the necessity for a blending model that extends to our target of a complex fluid.

Fig. 5.2(b) shows several measurements of other mixtures and the corresponding fittings. From the measured dotted data and fitted solid line, we can see that the flowing behavior of the mixtures can also be nicely fitted by the Herschel-Bulkley model as well. This shows that the material property of our target, pure fluid and mixture, can be described by the Herschel-Bulkley parameter, regardless of the differences in their internal elements. Hence, we will consider constructing our blending model that is closed in the space of the Herschel-Bulkley model and reproduce the measured data of the mixture.

5.3 Blending model for the mixture of complex fluid

We need a new blending model that can represent the mixture of complex fluid inside the Herschel–Bulkley parameter space from known pure material parameters and mixing ratio.

However, such a model is not an arbitrary function that uses pure material properties and mixing ratio as arguments. There are several laws that should be satisfied for a model to represent mixing. For example, when the $\alpha = 0$ or $\alpha = 1$, the model reduce the pure material. When three different fluids are mixed, the properties of the mixture should be constant irrespective of the order of mixing. Therefore, we will look for a form of a blending model that can be applied in terms of what laws should be satisfied with respect to the operation of mixing.

5.3.1 The formulation of the blending model

For the sake of simplicity, we assume that the blending process is both mass and volume conserving. Mathematically, we characterize a substance $\mathbb{S}$ by its mass m and a set of material parameters $\boldsymbol{M}$, i.e., $\mathbb{S} := (m, \boldsymbol{M})$. A blending model defines how a substance $\mathbb{S}_C$ can be represented by its constituents, for instance. For instance $\mathbb{S}_A$ and $\mathbb{S}_B$, defining the operator $\otimes$, we have $\mathbb{S}_C = \mathbb{S}_A \otimes \mathbb{S}_B$. We ask that a blending model satisfies a set of consistency properties.

In the field of chemistry, Rusin [78] introduced five such properties for octane numbers blending and introduced the mass conservation as an option (he called it additivity). He also showed that when we have the five properties, together with the additivity and the uniqueness in the decomposition, the blending operator $\otimes$ admits a general functional form (5.25).

Thus, our design of the nonlinear viscosity blending model is to make a particular choice of the functional form.

5.3.2 Laws of blending

Following the five properties about the mixing of Rusin [78] and the mass conservation, We consider the following six laws of blending; (1) Commutative law, (2) Distributive law, (3) Zero law, (4) Associative law, (5) Identity law, and (6) Mass conservation law.
(1) Commutative law states that the left and right hand sides of the operator $\otimes$ are interchangeable, or equivalently, that blending $\mathbb{S}_A$ to $\mathbb{S}_B$ and blending $\mathbb{S}_B$ to $\mathbb{S}_A$ should result in the same substance:

$$(m_A, \boldsymbol{M}_A) \otimes (m_B, \boldsymbol{M}_B) = (m_B, \boldsymbol{M}_B) \otimes (m_A, \boldsymbol{M}_A). \tag{5.10}$$

(2) Distributive law states that multiplying the masses of the constituents with the same factor k will result in a substance with the mass scaled in the same factor k but without changing the material property, i.e., if the following equation holds for $k = 1$, then it holds for any positive $k > 0$:

$$(km_A, \boldsymbol{M}_A) \otimes (km_B, \boldsymbol{M}_B) = (km_C, \boldsymbol{M}_C). \tag{5.11}$$

(3) Zero law states that mixing a substance of positive mass ($m_A > 0$) with any material of *zero* mass ($m_B = 0$) has no effect:

$$(m_A, \boldsymbol{M}_A) \otimes (0, \boldsymbol{M}_B) = (m_A, \boldsymbol{M}_A). \tag{5.12}$$

(4) Associative law states that an application of a sequence of blending operations would result in the same substance, regardless of the (associative) order of the operations:

$$\begin{aligned} &((m_A, \boldsymbol{M}_A) \otimes (m_B, \boldsymbol{M}_B)) \otimes (m_C, \boldsymbol{M}_C) \\ &= (m_A, \boldsymbol{M}_A) \otimes ((m_B, \boldsymbol{M}_B) \otimes (m_C, \boldsymbol{M}_C)) \,. \end{aligned} \tag{5.13}$$

Together with the commutative law, the associative law states that the result of the mixing does not depend on the path (or order) of blending. This is considered to be a natural characteristic we would ask physically, especially in the absence of chemical reactions.
(5) Identity law states that mixing two substances with the same material would result in a substance with the identical material and the summed total mass:

$$(m_{A1}, \boldsymbol{M}_A) \otimes (m_{A2}, \boldsymbol{M}_A) = (m_{A1} + m_{A2}, \boldsymbol{M}_A). \tag{5.14}$$

(6) Mass conservation law, in the case of a closed system without nuclear reactions, it is natural to ask in closed system:

$$(m_A, \boldsymbol{M}_A) \otimes (m_B, \boldsymbol{M}_B) = (m_A + m_B, \boldsymbol{M}_C). \tag{5.15}$$

5.3.3 General blending model satisfying the laws of blending

Combining the mass conservation law (5.15) with the distributive law (5.11), setting $k = \frac{1}{m_A+m_B}$, and letting $\alpha = \frac{m_A}{m_A+m_B}$, we have

$$(\alpha, \boldsymbol{M}_A) \otimes (1-\alpha, \boldsymbol{M}_B) = (1, \boldsymbol{M}_C), \tag{5.16}$$

where α represents the mixing ratio. Eq. (5.16) implies that the mixed material $\boldsymbol{M}_C$ can be represented as a map $\boldsymbol{G}$ of just mixing ratio α and material $\boldsymbol{M}_A$, $\boldsymbol{M}_B$:

$$\boldsymbol{M}_C = \boldsymbol{G}(\alpha, \boldsymbol{M}_A, \boldsymbol{M}_B). \tag{5.17}$$

As we expected, the laws of blending can be recasted as a set of laws on $\boldsymbol{G}$. The commutative law can be recasted as:

$$\boldsymbol{G}(\alpha, \boldsymbol{M}_A, \boldsymbol{M}_B) = \boldsymbol{G}(1-\alpha, \boldsymbol{M}_B, \boldsymbol{M}_A). \tag{5.18}$$

The distributive law is already incorporated to the form of $\boldsymbol{G}$, through the usage of the mixing ratio (rather than mass) as the first argument. The zero law can be recasted as, $\alpha = 0$ or $\alpha = 1$:

$$\boldsymbol{G}(0, \boldsymbol{M}_A, \boldsymbol{M}_B) = \boldsymbol{M}_B, \tag{5.19}$$

$$\boldsymbol{G}(1, \boldsymbol{M}_A, \boldsymbol{M}_B) = \boldsymbol{M}_A. \tag{5.20}$$

The associative law can be recasted as:

$$\begin{aligned} &\boldsymbol{G}\left(\frac{m_A+m_B}{m_A+m_B+m_C}, \boldsymbol{G}\left(\frac{m_A}{m_A+m_B}, \boldsymbol{M}_A, \boldsymbol{M}_B\right), \boldsymbol{M}_C\right) \\ =&\boldsymbol{G}\left(\frac{m_A}{m_A+m_B+m_C}, \boldsymbol{M}_A, \boldsymbol{G}\left(\frac{m_B}{m_B+m_C}, \boldsymbol{M}_B, \boldsymbol{M}_C\right)\right). \end{aligned} \tag{5.21}$$

The identity law can be recasted as, $\boldsymbol{M}_A = \boldsymbol{M}_B = \boldsymbol{M}$:

$$\boldsymbol{G}(\alpha, \boldsymbol{M}, \boldsymbol{M}) = \boldsymbol{M}. \tag{5.22}$$

The family of $\boldsymbol{G}$

The family $\mathcal{G}$ of this map $\boldsymbol{G}$ is a general function space of blending that includes the standard linear blending model $\boldsymbol{L} \in \mathcal{G}$:

$$\boldsymbol{M}_C := \boldsymbol{L}(\alpha, \boldsymbol{M}_A, \boldsymbol{M}_B) = \alpha \boldsymbol{M}_A + (1-\alpha)\boldsymbol{M}_B, \tag{5.23}$$

as well as the multiplicative blending model $\boldsymbol{X} \in \mathcal{G}$:

$$\boldsymbol{M}_C := \boldsymbol{X}(\alpha, \boldsymbol{M}_A, \boldsymbol{M}_B) = \boldsymbol{M}_A^{\alpha} \odot \boldsymbol{M}_B^{(1-\alpha)}, \tag{5.24}$$

where $\odot$ indicates the componentwise multiplication, and the power is defined in a componentwise manner as well. Rusin [78] pointed out a general class of the family $\mathcal{G}$ in the form:

$$\boldsymbol{M}_C = \boldsymbol{G}(\alpha, \boldsymbol{M}_A, \boldsymbol{M}_B) := \boldsymbol{F}^{-1}(\alpha \boldsymbol{F}(\boldsymbol{M}_A) + (1-\alpha)\boldsymbol{F}(\boldsymbol{M}_B)), \tag{5.25}$$

where $\boldsymbol{F}$ is an arbitrary invertible map that preserves the dimensionality of the material parameters.

In fact, setting $\boldsymbol{F}$ to the identity map $\boldsymbol{I}(\boldsymbol{M}) = \boldsymbol{M}$, and $\boldsymbol{I} = \boldsymbol{I}^{-1}$, it recover the linear blending model (5.23),

$$\begin{aligned} \boldsymbol{M}_C &= \boldsymbol{I}^{-1}(\alpha \boldsymbol{I}(\boldsymbol{M}_A) + (1-\alpha)\boldsymbol{I}(\boldsymbol{M}_B)) && (5.26)\\ &= \alpha \boldsymbol{M}_A + (1-\alpha)\boldsymbol{M}_B. && (5.27) \end{aligned}$$

With the componentwise logarithmic map $\boldsymbol{F}(\boldsymbol{M}) = \log \boldsymbol{M}$, $\boldsymbol{F}^{-1}(\boldsymbol{M}) = e^{\boldsymbol{M}}$, we recover the multiplicative blending model (5.24),

$$\begin{aligned} \boldsymbol{M}_C &= e^{\alpha \log(\boldsymbol{M}_A) + (1-\alpha)\log(\boldsymbol{M}_B)} && (5.28)\\ &= \left(e^{\log(\boldsymbol{M}_A)}\right)^{\alpha} \odot \left(e^{\log(\boldsymbol{M}_B)}\right)^{1-\alpha} && (5.29)\\ &= \boldsymbol{M}_A^{\alpha} \odot \boldsymbol{M}_B^{1-\alpha}. && (5.30) \end{aligned}$$

5.4 Our nonlinear blending model

Now, our aim is to find the map $\boldsymbol{F}(\boldsymbol{M})$ generate the blending model that can represent material blended from a wide variety of material properties, which are described by the three Hershel-Bulkley parameters (η_H,n_H,σ_{HY}) as its arguments. We used the data-driven fitting approach to find the map $\boldsymbol{F}(\boldsymbol{M})$ from the measured data. We show later that by blending the three parameters in a nonlinear way, it becomes possible to reproduce the characteristic behavior shown in Fig. 5.1 that are impossible to describe when only considering blending for effective viscosity (i.e., the blending of viscosity for each particular shear rate).

5.4.1 Data-driven approach to obtain the model

Our viscosity blending model $\hat{\boldsymbol{F}}$ reproduce the estimated material parameters $(\hat{\eta}_H, \hat{n}_H, \hat{\sigma}_H)$ at mixing ratio α,

$$\hat{\mathbf{F}} \begin{pmatrix} \hat{\eta}_H \\ \hat{n}_H \\ \hat{\sigma}_{HY} \end{pmatrix} = \alpha \hat{\boldsymbol{F}} \begin{pmatrix} \eta_{H,A} \\ n_{H,A} \\ \sigma_{HY,A} \end{pmatrix} + (1-\alpha)\hat{\boldsymbol{F}} \begin{pmatrix} \eta_{H,B} \\ n_{H,B} \\ \sigma_{HY,B} \end{pmatrix}, \tag{5.31}$$

where $\mathbf{M}_A = (\eta_{H,A}, n_{H,A}, \sigma_{HY,A})^\top$ and $\mathbf{M}_B = (\eta_{H,B}, n_{H,B}, \sigma_{HY,B})^\top$ are constituents, $(\cdot)^\top$ means transpose. We expect that the estimated parameters and the estimated flow curve match the fitted parameter and estimated flow curve from measured data of mixture at mixing ratio α, then we used the data of measured flow curves for five combinations of materials: mayo / honey, oyster sauce / honey, mayo / Japanese pork cutlet sauce, BBQ sauce / Mustard, and Worcestershire sauce / Japanese pork cutlet sauce.

As we seek the $\hat{\boldsymbol{F}}$ reproducing the limited number of measured data of mixtures, In order to construct our model that can reproduce the measured flow curve from the limited number of material samples, we limit the search space for the $\boldsymbol{F}$ map with three steps, rather than adopting a general form and fully making use of optimizations, which is an interesting future direction.

We start from 1) finding a function that works to blend the yield stress alone. Because the yield stress σ_{HY} is the only parameter related to the elasticity (it describes minimum shear stress when the fluid starts to flow and the limit of the elastic regime). The yield stress especially shows up at the low shear rate end of the flow curve. In concrete, we assume the following form for calculating the blended $\sigma_{HY,M}$ from that of the two constituents $\sigma_{HY,A}$ and $\sigma_{HY,B}$:

$$\sigma^p_{HY,M} = \alpha\sigma^p_{HY,A} + (1-\alpha)\sigma^p_{HY,B}, \tag{5.32}$$

where p is a parameter that we are going to seek. Note that it reduces to the multiplicative blending: $\sigma_{HY,M} = \sigma^\alpha_{HY,A}\sigma^{(1-\alpha)}_{HY,B}$ when $p \to 0$. By changing p, we computed the relative and absolute error between the estimated and the measured (fitted) values of $\sigma_{Y,M}$. As in Fig. 5.3(a), both errors produce negative p as the result of searching. But since having a value of $p < 0$ would cause undefined $\sigma_{Y,M}$ if one of $\sigma_{HY,A}$ and $\sigma_{HY,B}$ is zero, We adopted $p = 0$ as the value closest to the negative value [2] [3].

Next step 2), we are going to look at the high shear rate end, the flow curve in the logarithmic plot appears to be straight, with the slope characterized by the power parameter n_H. Thus, we try to find a function for solely blending the n_H parameter. In particular, we choose the following function space

$$n^q_{H,M} = \alpha n^q_{H,A} + (1-\alpha)n^q_{H,B}. \tag{5.33}$$

Like we did for the yield stress, we tested both relative and absolute errors between the estimated and the measured (fitted) values of n_H. As following the Fig. 5.3(b), $q = 0.6$ gives the smallest relative error, and $q = 1.4$ gives the smallest absolute error. For now, we keep both $q = 0.6$ and $q = 1.4$ for further inspection.

[2] We note that by making use a high-end machinery for more accurate measurements for the low shear rate regime would enable a finer inspection, which we leave as a future work.

[3] We did not use water as one of the constituents, as its nearly zero viscosity behavior at low shear rate regime turns out to be extremely hard to measure using our current device.

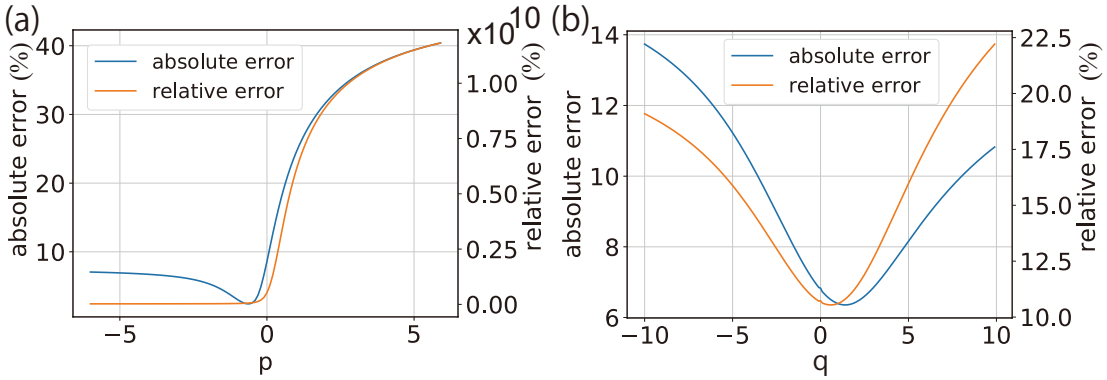

Figure 5.3: (a) The relative errors (orange line) and absolute errors (blue line) in predicting $\sigma_{HY,M}$ vs the parameter p. (b) The relative errors (orange line) and absolute errors (blue line) in predicting $n_{H,M}$ vs the parameter q. This figure is the reuse of the published article [66].

Finally, 3), we seek a way to estimate the η_H parameter for a mixture. We found that by taking the n_H parameter into account, we can nicely obtain the characteristic behavior in the η_H parameter that was observed from the measurements. We consider the $\boldsymbol{F}$ map with a parameter p ($p \to 0$) and q in the 1) and 2), it has the form

$$\hat{\boldsymbol{F}}((\eta_H, n_H, \sigma_{HY})^\top) = (\eta_H^{f(n_H)}, n_H^q, \ln \sigma_{HY})^\top, \tag{5.34}$$

where $f(n_H)$ is a parameter related to η_H taking n_H into account as a polynomial. For the space of $f(n_H)$, we tested the three forms $a + bn_H + cn_H^2$, $a/n_H + b + cn_H$, and $a/n_H^2 + b/n_H + c$. We enforced $f(1) = c$ so that our model reduces to one of the four empirical viscosity blending models ($c = -1$ for Bingham, $c = -0.384$ for Refutas, $c = 1$ for linear, and $c = 1/3$ for Kendall and Monroe). Because we have $q = 0.6$ and $q = 1.4$ from step 2), in total, we now have 24 candidates. For each of these cases, we considered both the absolute and relative errors in the estimated stress and optimized for the parameters a, b, and c. Then from these results, we first discarded models that gave absolute errors larger than 100%. This resulted in discarding the cases $c = 1$ and $c = 1/3$, as well as the form $a/n_H + b + cn_H$. Then, we selected the one with the smallest relative error for the rest of the models. This resulted in $q = 1.4$ and the following form for f:

$$f(n_H) = 0.12 - 3.2n_H + 2.7n_H^2. \tag{5.35}$$

As following the result through, finally, we obtained the map

$$\hat{\boldsymbol{F}}((\eta_H, n_H, \sigma_{HY})^\top) = (\eta_H^{0.12-3.2n_H+2.7n_H^2}, n_H^{1.4}, \ln \sigma_{HY})^\top. \tag{5.36}$$

We will confirm this our blending model generated by $\hat{\boldsymbol{F}}$ in a later results Section 5.5.

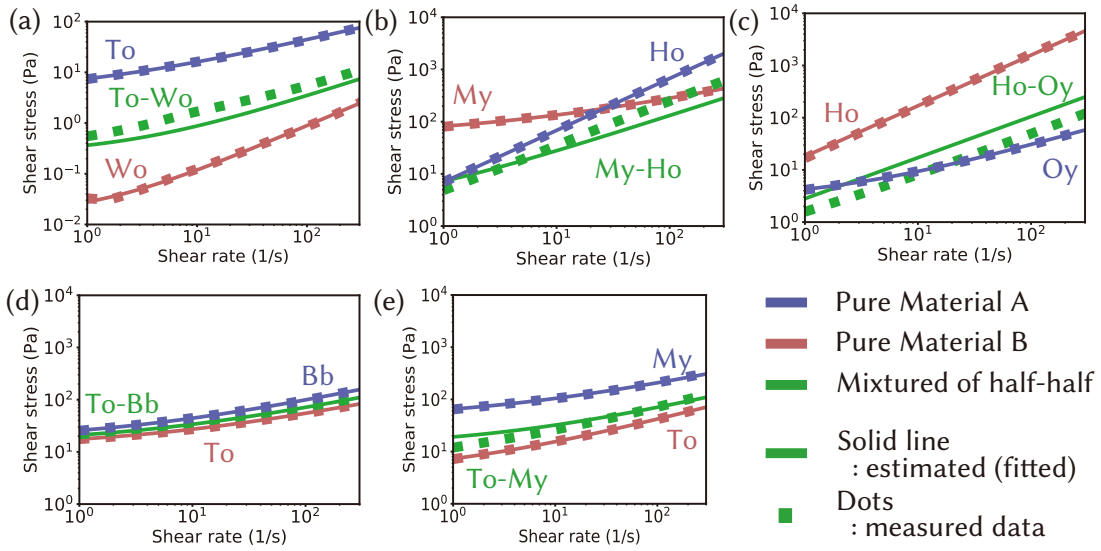

Figure 5.4: We show the flow curve to valid our blending model for several combination of mixture (a)∼(e), the measured data is shown in dots and the estimation is shown in solid line. blue and red correspond to the flow curve of pure constituents and green correspond to half-half blending. Our model qualitatively and nicely captures the characteristic behavior. This figure is the reuse of the published article [66].

5.5 Result and Discussion

We chose a blending model that can represent measured complex fluid mixtures among the general blending function derived from the mixing law using a data-driven approach, and we confirm the obtained model with flow-curve. In addition, we also validate the results by comparing real footage with the simulations.

5.5.1 Our blending model comparing the flow curve

We obtained our blending model given by the map $\hat{\boldsymbol{F}}$ with our data-driven approach. Using our model, we can estimate the Herschel–Bulkley parameters for the mixtures respective α we tested in an average of 55% absolute error.

In Fig. 5.4(a)∼(e), we compare the estimated flow curve with measured flow-curve, the dots show the measured data, and solid green lines show the estimated of the mixture at $\alpha = 0.5$ (red and blue are pure materials). We can observe the solid green line qualitatively agree with the dots. In Fig. 5.4(b), Mayo and Honey mixture, we can see that our model can describe the characteristic behavior of the viscosity decreasing since the estimated green line passes under the intersection of the curves of the pure materials. In Fig. 5.4(c), Honey and Oyster sauce mixture, the measured data shows that the green and blue dots line are close together and intersect at the small shear rate region. Our model can also describe this behavior. Considering that our tested

materials cover different types of rheological properties, including polymers, suspensions, and nearly Newtonian, we conclude that this is a nice approximation as the first step toward nonlinear blending.

5.5.2 Validation by simulation and real footage

We conduct experiments to observe how fluid flowing, using the nozzle to extrude the fluid on the slope; this experimental setup has been chosen to reproduce easily for the simulation. We loaded the specimen into a syringe and attached a silicone tube to it as for Fig. 5.5 (a). The other tip of the tube is attached to a 3D printed nozzle head for position alignment. In Fig. 5.5 (b) shows entire experimental apparatus. The syringe is pumped using a gear mechanism (manipulated by hand) for better control of the speed. The extruded specimen will fall onto a slanted aluminum plate. We use the first-generation iPhone SE camera to record the footage. The specimens are prepared by mixing two materials in the ratios 0% : 100%, 25% : 75%, 50% : 50%, 75% : 25%, and 100% : 0%, for different combinations of materials.

Then, we also replicated the nozzle and slope setup in our simulation, and we perform the MPM simulation on that setup to compare the results of the real footage [4]. In our simulation, the parameters for the pure materials, i.e., 0% : 100% and 100% : 0%, are taken from the measurements using our rheometer, and those for the mixtures are computed via our blending model using the mixing rate and the parameters for the pure materials.

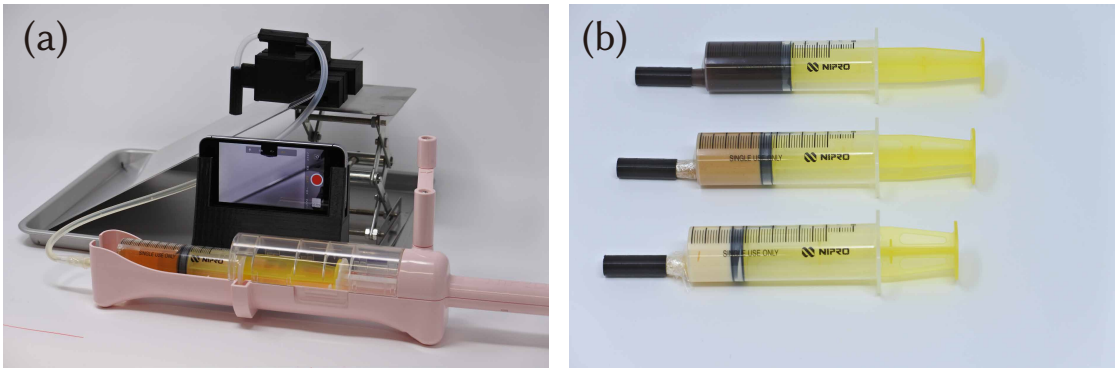

Figure 5.5: We shows the equipment for the nozzle experiment. (a) Our specimens to be extrude is prepared in syringes (b) The fluid in the syringe is pumped using a gear mechanism and transported to the nozzle above on the slope. We use the iPhone SE 1st generation for the footage recording. This figure is the reuse of the published article [66].

[4] All the simulations were run on an Amazon EC2 instance (c5-18xlarge, 72 cores of Intel (R) Xeon (R) Platinum 8124M 3GHz CPU). The code is parallelized using OpenMP, and each simulation used 12 cores. We did not intensively optimize our code. The number of material points in the simulation ranges around 100,000, and each frame (in 50 fps) took about 2 to 15 minutes.

Nozzle experiment in a binary mixture

We first performed tests for the combination of mayo and honey. As shown in Fig. 5.6(A)(a), the mixture of mayo and honey shows a much smoother flow, as opposed to the pure materials, which look less viscous and stack near the nozzle. This behavior is nicely captured using our model as shown in Fig. 5.6(A)(d), and cannot be captured as shown in Fig. 5.6(A)(b) and (c). (b) is a result of using a linear blending model. (c) shows the blending by initializing the material points using randomized binary labels (for mayo and honey) and computing the stress by summing up the per-particle stress computed using parameters for the pure materials (we call the latter a standard MPM in the sequel). Fig. 5.6(B) shows the pixel length from the fluid edge to bottom with each times of each mixtures 75 : 25, 50 : 50, 25 : 25 Fig. 5.6(B) shows the pixel length from the liquid edge to the bottom at each time for 75 : 25, 50 : 50, and 25 : 25 mixtures as an evaluation for reference. The red dots is length from real footage, the blue dots is from linear blending result, and the orange dots is from our blending model results. We can observe that orange dots line nicely agrees with the red dots line.

Fig. 5.7(A)(a)∼(d) shows the result of the test for the combination of mayo and Japanese port cutlet sauce. Like the combination of honey and mayo, the mixed materials flow smoothly. Our model, as shown in (d), can also capture this behavior, whereas the linear blending model and a standard MPM simulation with randomized material labels cannot, as shown in (b) and (c). As shown in Fig. 5.7(B), we can observe that orange dots line more agree with the red dots line.

Then, we performed tests for the combination of oyster sauce and honey in Fig. 5.8(a)-(d). Again, we observe that with linearly blended material parameters or a standard MPM simulation with randomized material labels, the flows of the intermediate mixing ratios are much slower than the footage. Our nonlinear blending model provides smooth flow. We also observed a mismatch between the simulated and captured examples for the 50 : 50, 75 : 25 % blend, and pure oyster sauce. We believe this is due to the lack of surface tension in our simulation (surface tension was not incorporated into our MPM simulation). The pure oyster sauce flowed down the slope without spreading in the transverse direction, whereas the simulated one did due to the absence of surface tension. Since the main focus was to treat viscosity, let the incorporation of surface tension be as future work. The result of Fig. 5.7(B) reflect this mismatch, however, we can observe that the orange dots line more agree than blue dots line with the red dots line.

Nozzle experiment in a mixture of three

Our proposed model satisfies the law of mixtures, i.e., it satisfies distributive law. Therefore, for more than two mixtures, our model is valid, without the undesired dependence of the properties of the mixture on the order of mixing.

We tested if our model could be applied to a mixture of the three materials, such

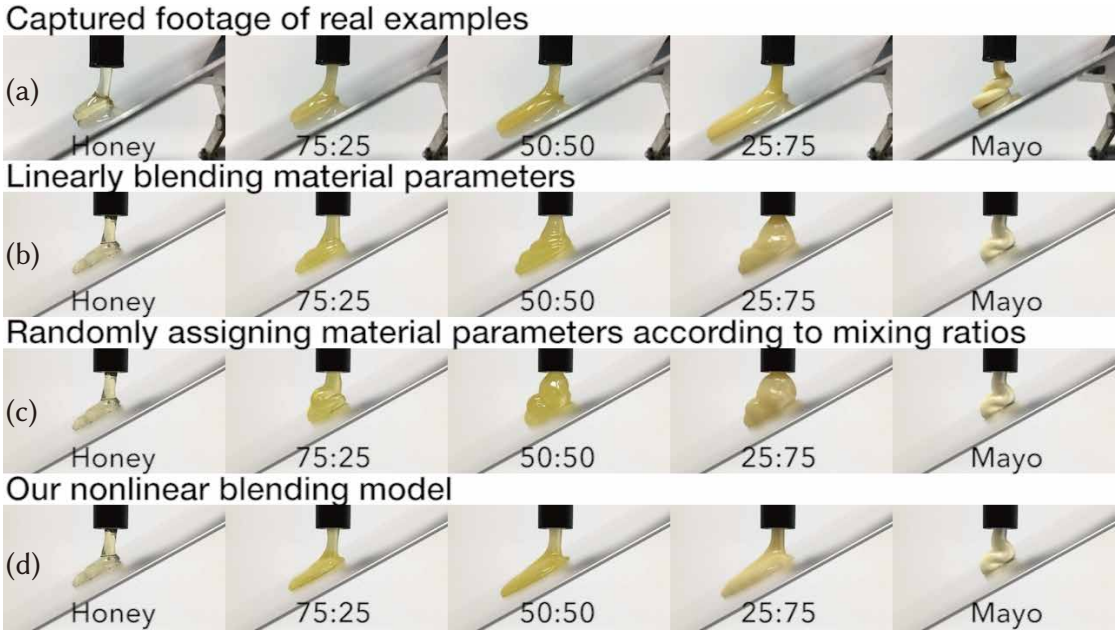

(A) The caputerd footage of mayo (ho) and honey sauce at 0.5s

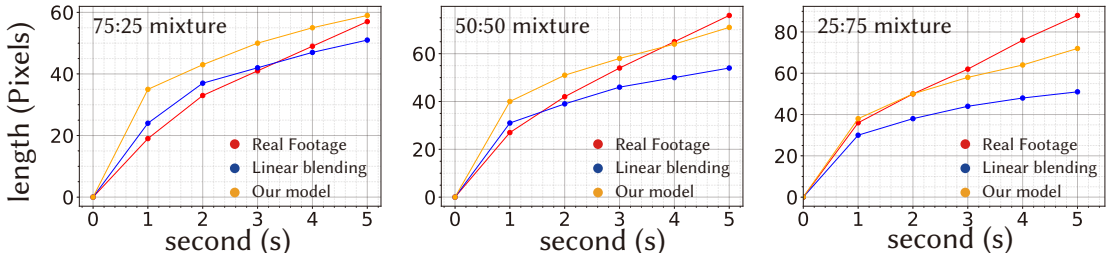

(B) The length (Pixels) from edge to bottom vs times

Figure 5.6: (A) Nozzle experiment in a binary mixture of Honey and Mayo. (a) the result of captured real footage. (b): the result of using a linear blending model. (c): the blending by by initializing the material points using randomized binary labels (for mayo and honey) and computing the stress by summing up the per-particle stress computed using parameters for the pure materials (we call the latter a standard MPM in the sequel). (d): using our non-linear blending model. This figure is the reuse of the published article [66]. (B) We also shows the pixel length from the fluid edge to bottom with each times of each mixtures $75:25$, $50:50$, $25:25$.

as mustard, mayo, and honey. The space of the mixture forms a triangle as in Fig. 5.9. The experimental settings of the real experiments follow the previous section. In our simulation, the material parameters of the mixtures are estimated from only the three pure materials, and our model works well for this mixture of three materials.

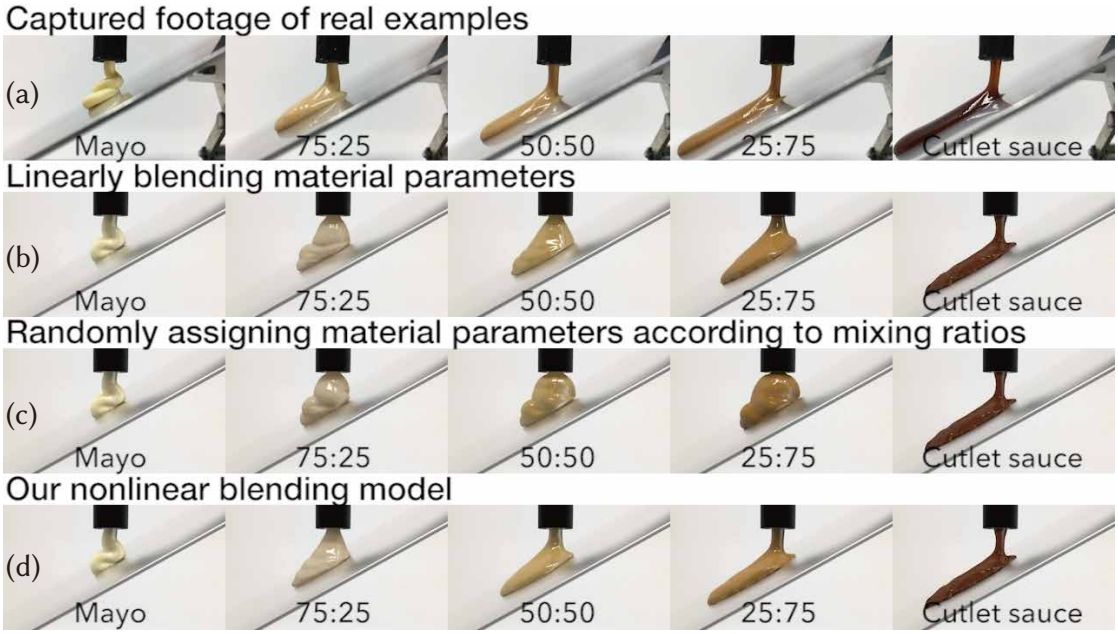

(A) The caputerd footage of mayo (ho) and Japanese pork cutlet sauce at 0.5s

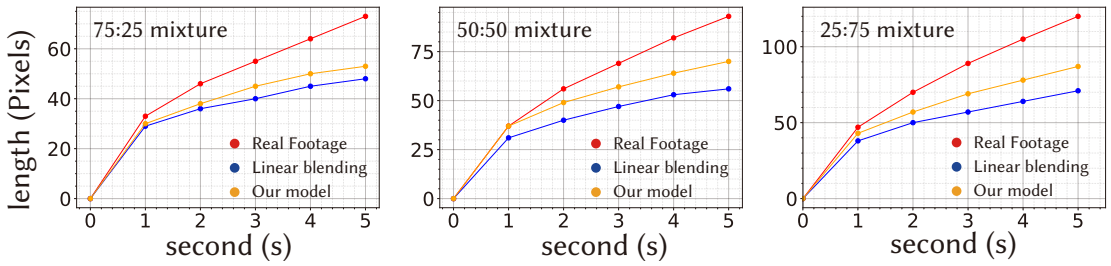

(B) The length (Pixels) from edge to bottom vs times

Figure 5.7: (A) We observe the flow behavior of mixtures of mayo (My) and Japanese pork cutlet sauce (To). (a) A captured footage of the mixtures with various mixing ratios. (b) MPM simulation using linearly blended material parameters. (c) A standard MPM simulation with randomized material labels. (d) MPM simulation with our non-linear blending model. our non-linear blending model can qualitatively capture the flow behavior of real footage by looking at the edge positions of the fluid. This figure is the reuse of the published article [66]. (B) We also shows the pixel length from the fluid edge to bottom with each times of each mixtures $75:25$, $50:50$, $25:25$.

5.5.3 Our model limitation

There are several limitations and future directions of our model. First, we have not considered the blending of elasticity; In our simulation to compare, we assumed all the materials have a same bulk modulus $\kappa = 10^6 Pa$, and a same shear modulus $\mu = 10^5 Pa$. Second, the accuracy for $n_H < 0.4$, $n_H \geq 1.0$, and the case of extremely low and high shear rates need further investigation. We also point out that the identity rule and the associative rule may not always hold from the perspective of rheology (e.g.,

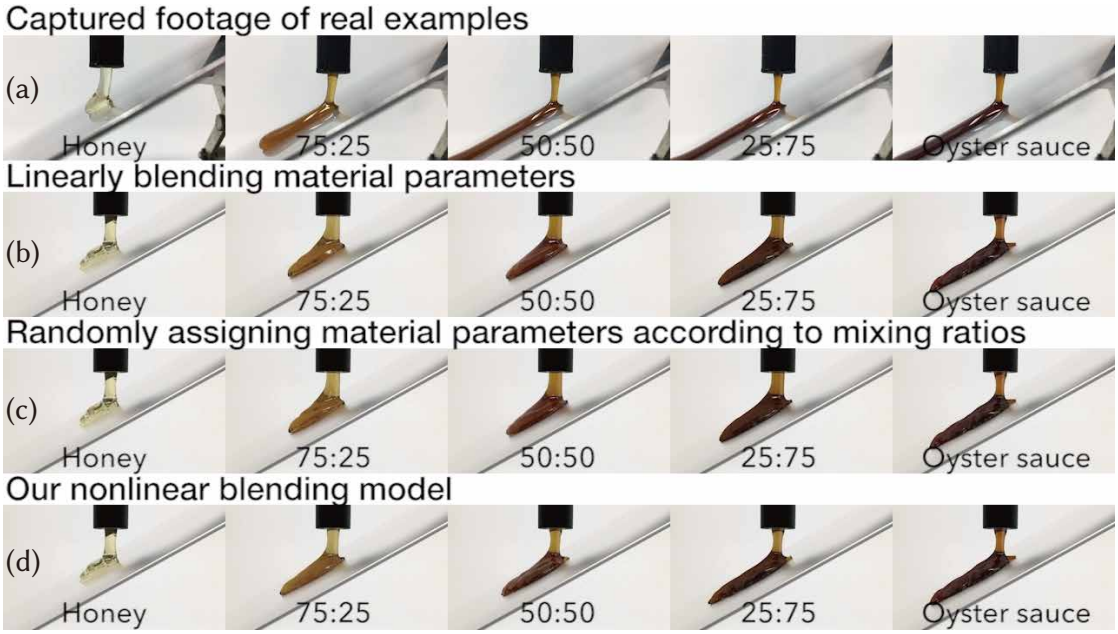

(A) The caputerd footage of Honey (ho) and Oyster sauce at 0.3s

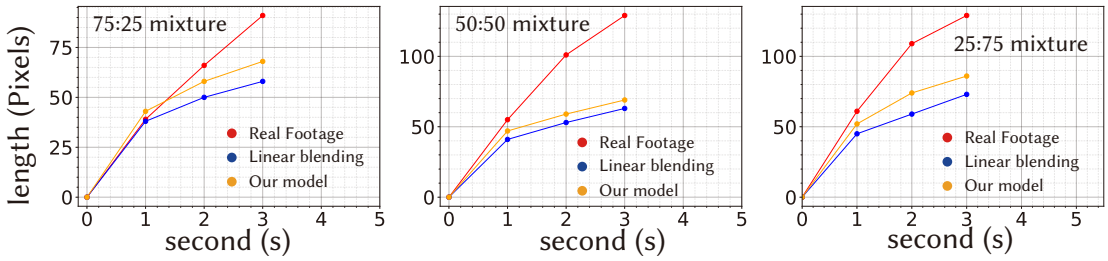

(B) The length (Pixels) from edge to bottom vs times

Figure 5.8: (A) We observe the flow behavior of mixtures of Honey (ho) and Oyster sauce (Oy). (a) A captured footage of the mixtures with various mixing ratios. (b) MPM simulation using linearly blended material parameters. (c) A standard MPM simulation with randomized material labels. (d) MPM simulation with our non-linear blending model. This figure is the reuse of the published article [66]. (B) We also shows the pixel length from the fluid edge to bottom with each times of each mixtures $75:25$, $50:50$, $25:25$.

suspension flows with different particle distributions). But the fact that the model can nicely represent the captured flow curve is an encouraging fact, implying that our $\boldsymbol{F}$ map is a good approximation. A 'second order' binary mixture model might be interesting as a follow up work to improve the accuracy.

5.6 Summary and conclusions

We found the flow curve of the various fluid-like foods and their mixture as several classes of complex fluid can be nicely fitted by Herschel–Bulkley model, i.e., the Herschel-

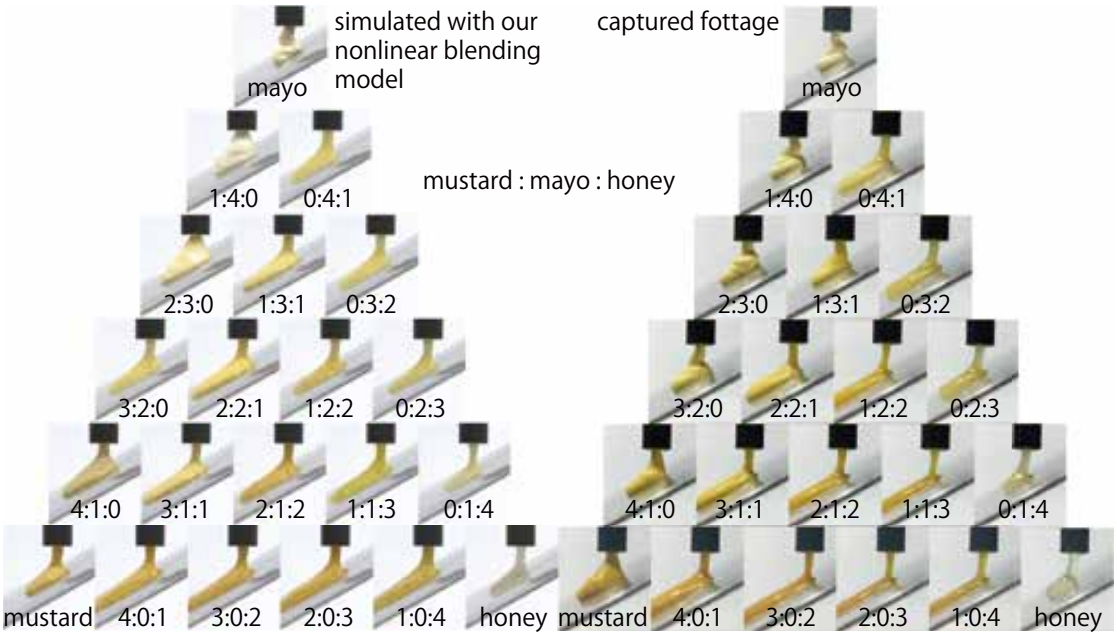

Figure 5.9: Nozzle experiment in mixture of three different materials, mustard : mayo : honey, the result of each is placed in a triangle. Left: simulated with our nonlinear blending model. Right: captured footage from our experiment. This figure is the reuse of the published article [66].

Bulkley parameter can characterize the material property of them. By studying the mixing law, which mathematically formulation of the several conditions in the mixing process, we introduce the general blending model. We applied the Herschel–Bulkley parameter to the general blending model, and we chose and constructed the nonlinear viscosity blending model that can reproduce the measured mixture data as a data-driven fitting approach. Our model can nicely capture intriguing and unintuitive behavior, such as the mixture of honey and mayo. Besides the immediate benefit of our research on simulating dynamical mixing of multiple fluids (e.g., for cooking), our model can provide a nice initial guess for the material property of an unmeasured mixture with known parameters, and can represent the various mixture of complex fluids having a quite different underlying microscopic structure (emulsions, polymers, colloidal suspensions, etc.), this is also interesting because whether the model satisfies the mixing law exists is not trivial.

Our method via the general blending model and data-driven fitting approach has potentially wider application than what we have covered in this thesis. We emphasize that this methodology is also effective in acquiring the blending model for the wider or specific targets. If we have the pure and mixture measuring data for the targets, we will obtain the model that satisfies the mixing law. Therefore, the measuring data of flow curves is necessary and important, and the necessity of the rheometer as a measuring device is considered as the limitation. In general, a rheometer with a practical accuracy

(like ours) is expensive ($50k$) and time-consuming, so the acquisition of the data of flow curve is one of the problems. We treat this problem in Chapter 6.

Chapter 6

Video-based convenient measurement method for complex fluid by solving the inverse problem via a simulation

本章については，5 年以内に雑誌等で刊行予定のため、非公開。

Chapter 7

Conclusion

Simulation and data-driven approaches are used to analyze and propose practical applications for the reproduction and measurement of a wide class of complex fluids.

In Chapter 4, we explored the limits of reproducing the solid-like properties of complex fluids and the unclear physical behavior around the limit. The solid-like behavior of fluid are related to the jamming transition phenomenon, which phenomenon is a qualitative change of the from fluid-like to solid-like state depending on the density of the internal elements. We will focus on the density dependence, especially around the jamming transition density φ_{J}, of the Reversivle-Irreversivle (RI) transition relating the particle trajectory under the oscillatory shear, which may be related to the jamming phenomena. In order to investigate this, we use the athermal colloidal system with oscillatory sheared, which is a simple model that can reproduce and investigate these phenomena and the RI transition behavior numerically. In particular, there are few studies that have investigated the behavior of the RI transition across the jamming transition density in detail, and the relationship between the transition behavior, mechanical properties such as elastic, and particle structure is unclear. Thus, we investigate these issues by conducting exhaustive numerical simulation at various particle densities and shear amplitudes. As a result, a phase diagram of the RI transition around the jamming transition density in a colloidal particle system with shear is obtained. Based of this phase diagram, we observed that there are richer physical phenomena than we expected around the Jamming transition density region, such as the non-trivial RI transition below φ_{J} and the nonlinear elastic region, and that RI transition can be related to the yilding transition (changing solid-state to fluid-state by applying shear) and the contacts number reflecting the particle structure.

In Chapter 5, to reproduce the nonlinear viscosity of complex fluids, we aim to find a method for reproducing and estimating the nonlinear viscosity of the mixture of complex fluid. In this thesis, we want to reproduce the mixing of various classes of fluids irrespective of the internal elements and the structure. Therefore, from a macroscopic point of view, we investigated the possibility of methods and techniques to handle the reproduction of mixtures by only using the macroscopic property. We observed that

the flow curves, which represent the flowing behavior, can characterize the various fluids and their mixtures by the Harshall-Bulkley model. Hence, we consider a blending model closed by the parameters of the Harshall-Bulkley model, which reproduces the physical properties of the mixture from the pure fluids and the mixing ratio. We introduce laws of blending as an axiomatic system, which is a mathematical formulation of the condition satisfying the process of mixing and define the family of function that satisfies this laws of blending as a general blending model. By using the data-driven fitting approach, we chosen the blending model that can reproduce the mixture data among the general blending model. The acquired model was shown to be capable of reproducing the characteristic behavior complex fluid mixtures, and we also validate the effectiveness of our model by comparing macroscopic fluid simulations with actual experiments video.

In Chapter 6, we proposed a video-based measurement method for conveniently measuring the flowing behavior of complex fluids that can be used by non-specialists. Although fluids with various and rich properties are very familiar to us, the method to measure with accurate them is not common because it requires a mechanical experimental device called a rheometer, which is expensive $50k$ dollars (our rheometer) and needs expert knowledge. For more effective modeling and understanding of complex fluids, it is necessary to collect more data of various class of complex fluids, and this convenient measurement methods encourage this. Physical property measurement corresponds to the inverse problem of the forward problem of reproducing a certain physical property. We interpret the existing video-based viscosity measuring method for Newtonian as a method based on the numerical solution of the inverse problem by combining a fluid simulation and optimization. Extending it to the complex fluids as Herschel–Bulkley model, we proposed a method for estimating and measuring the flow curve of various classes of complex fluids from the experimental videos. In addition, by introducing a similarity structure of physical properties, we proposed a method to evaluate effective experimental setups to capture the fluid video for estimation and to propose new setups. These proposed methods were tested on artificial data and real experimental data. First, the effectiveness of the proposed setup was verified by using a toy model with the velocity field of the Hagen-Poiseuille flow as the input instead of a fluid video. Secondly, we used an artificial fluid video given by two-dimensional simulation as an input to verify whether it is possible to estimate the flow curve of a complex fluid from a fluid video. Finally, we confirmed the effectiveness of the proposed method by comparing the results of estimation from the real experimental video with the measured data via the rheometer.

The results of this thesis show that the appropriate use of numerical simulation and data-driven methods can provide effective methods and new insights for complex fluids that are apparently difficult to reproduce or measure by analysis. Comprehending the effectiveness of these approaches will give us more options for various approaches to complex fluids and systems, and consequently expect to enable us to understand and

apply complex fluids from various perspectives and viewpoints.

Acknowledgements

First of all, I would like to express my deep appreciation to all people in this world, the nature, the Sacred, and gods. I realized that I am very blessed to have been able to write this thesis, do this research, and be here. I recognize and understand that I am living my life with the support and help of many people. This is the most valuable thing for me.

I would like to express my sincere gratitude to my supervisor Professor Masato Okada. He always encouraged me and gave me insightful advice and comment during this five years. I learned not only technical features but also how to live in this world from his comment, word, and his behavior.

I am deeply grateful to Associate Professor Yonghao Yue (Now, Aoyama Gakuin University). I would never have been able to grow or gain anything without his grateful support. His deep insights, idea, and words, e.g., technical issues, how to treat the task, writing and speaking, mental keeping, methodology, always gave me great inspiration and multiple perspectives and have helped me grow a lot.

I would like to offer my special thanks to Professor Kunimasa Miyazaki in Nagoya University. In addition to his support for my research, his talks on physics have given me various insights and surprises and helped me to realize interest of soft matter, Non-equilibrium physics. I would like to express my special thanks to Professor Takeshi Kawasaki in Nagoya University. I didn't know anything about rheology at the time, but he gave me a very detailed lecture and an exciting idea. Thanks to his great support and encouragement, I was able to complete my research after graduating from Nagoya University.

I would like to thank all members of my Ph.D. committee, Professor Osamu Yamamuro, Professor Akira Ejiri, Professor Yoshiyuki Kabashima, Professor Chikara Furusawa, and Professor Naoki Kawashima, for providing valuable comments on my drafts and presentation for this thesis.

I am gratefully thankful to all members of Okada laboratory. There have been too many to count, but I would like to mention the names, Mr.Takayuki Suzuki, who helped me the experiment of research in mixing, Assistant Professor Shun Katakami who gave me great advice for editing and preparing this Ph.D. thesis. I would like to express my special thanks to Professor Ryohei Seto (University of Chinese Academy of Sciences), who discussed and gave me physics insight in the research of mixing.

Let me remark that my Ph.D. course was financially supported entirely by Japan Society for the Promotion of Science (JSPS)

Finally, I would like to express my profound gratitude to my family, especially my mother Miyuki, my father Shuichi, my brother Ryoji. I am a fool and non-valuable person, but they have always encouraged, supported, entertained, and trusted me. Moreover, they have been lived happy and in good health. Thanks to them, I have lived and done what I want to do until today.

I am really blessed, and I would like to return the favor. I hope that accomplishing this thesis will be one of them.

References

[1] Michael P. Allen. *"Computer simulation of liquids"*. edition, 1987.

[2] American Society for Testing and Materials. *ASTM D7152 11: Standard Practice for Calculating Viscosity of a Blend of Petroleum Products*, 2016.

[3] Svante Arrhenius. Über die dissociation der in wasser gelösten stoffe. *Zeitschrift für Physikalische Chemie*, 1U(1):631–648, 1887.

[4] Howard A. Barnes. An examination of the use of rotational viscometers for the quality control of non-newtonian liquid products in factories. *Appl. Rheol.*, 11(2):89–101, April 2001.

[5] Aaron S. Baumgarten, Benjamin L.S. Couchman, and Ken Kamrin. A coupled finite volume and material point method for two-phase simulation of liquid–sediment and gas–sediment flows. *Comput. Methods Appl. Mech. Eng.*, 384:113940, October 2021.

[6] Elena Bayod, Ene Pilman Willers, and Eva Tornberg. Rheological and structural characterization of tomato paste and its influence on the quality of ketchup. *LWT - Food Science and Technology*, 41(7):1289–1300, September 2008.

[7] Eugene C. Bingham and Delbert F. Brown. The mixture law. *Journal of Rheology*, 3(1):95–112, 1932.

[8] Guillaume Chatté, Jean Comtet, Antoine Niguès, Lydéric Bocquet, Alessandro Siria, Guylaine Ducouret, François Lequeux, Nicolas Lenoir, Guillaume Ovarlez, and Annie Colin. Shear thinning in non-brownian suspensions. *Soft Matter*, 14(6):879–893, February 2018.

[9] Jingyu Chen, Victoria Kala, Alan Marquez-Razon, Elias Gueidon, David A B Hyde, and Joseph Teran. A momentum-conserving implicit material point method for surface tension with contact angles and spatial gradients. *ACM Transactions on Graphics*, 40(4):1–16, July 2021.

[10] Laurent Corté, P. M. Chaikin, J. P. Gollub, and D. J. Pine. "Random organization in periodically driven systems". **4**:420–424, 2008.

[11] Philippe Coussot and Jean - michel Piau. A large - scale field coaxial cylinder rheometer for the study of the rheology of natural coarse suspensions. *J. Rheol.*, 39(1):105–124, January 1995.

[12] Simon Dagois-Bohy, Ellák Somfai, Brian P. Tighe, and Martin van Hecke. Softening and yielding of soft glassy materials. *Soft Matter*, 13:9036–9045, 2017.

[13] Olivier Darrigol. *Worlds of Flow, A history of hydrodynamics from the Bernoullis to Prandtl*. Oxford University Press, 2008.

[14] Pallabi Das, H. A. Vinutha, and Srikanth Sastry. Unified phase diagram of reversible–irreversible, jamming, and yielding transitions in cyclically sheared soft-sphere packings. *Proc. Natl. Acad. Sci. U. S. A.*, 117(19):10203–10209, May 2020.

[15] Gilles Daviet and Florence Bertails-Descoubes. A semi-implicit material point method for the continuum simulation of granular materials. *ACM Transactions on Graphics (Proc. of SIGGRAPH 2016)*, 35(4):102:1–13, 2016.

[16] P. G. De Gennes. Reptation of a polymer chain in the presence of fixed obstacles. *The Journal of Chemical Physics*, 55(2):572–579, 1971.

[17] Antoine Deblais, Elyn den Hollander, Claire Boucon, Annelies E Blok, Bastiaan Veltkamp, Panayiotis Voudouris, Peter Versluis, Hyun-Jung Kim, Michel Mellema, Markus Stieger, Daniel Bonn, and Krassimir P Velikov. Predicting thickness perception of liquid food products from their non-newtonian rheology. *Nat. Commun.*, 12(1):6328, November 2021.

[18] Murat Dervisoglu and Jozef L. Kokini. Steady Shear Rheology and Fluid Mechanics of Four Semi - Solid Foods. *Journal of Food Science*, 51(3):541–546, 1986.

[19] Masao Doi and Sam. Edwards. *The Theory of Polymer Dynamics*. Oxford Univ Press, 1988.

[20] D. J. Durian. Foam mechanics at the bubble scale. *Phys. Rev. Lett.*, 75(26):4780–4783, December 1995.

[21] S. F. Edwards. The statistical mechanics of polymerized material. *Proceedings of the Physical Society*, 1967.

[22] S. F. Edwards and Masao Doi. Dynamics Of Concentrated Polymer Systems Part 3. *Journal of the Chemical Society, Faraday Transactions 2: Molecular and Chemical Physics*, 74:1818–1832, 1978.

[23] A. Einstein. Eine neue bestimmung der moleküldimensionen. *Annalen der Physik*, 324(2):289–306, 1906.

[24] Randy H Ewoldt and Chaimongkol Saengow. Designing complex fluids. *Annu. Rev. Fluid Mech.*, January 2022.

[25] Yu Fang, Minchen Li, Ming Gao, and Chenfanfu Jiang. Silly rubber: an implicit material point method for simulating non-equilibrated viscoelastic and elastoplastic solids. *ACM Transactions on Graphics*, 2019.

[26] Yu Fang, Ziyin Qu, Minchen Li, Xinxin Zhang, Yixin Zhu, Mridul Aanjaneya, and Chenfanfu Jiang. IQ-MPM: an interface quadrature material point method for non-sticky strongly two-way coupled nonlinear solids and fluids. *ACM Transactions on Graphics*, 2020.

[27] Behrooz Ferdowsi, Michele Griffa, Robert A Guyer, Paul A Johnson, Chris Marone, and Jan Carmeliet. Acoustically induced slip in sheared granular layers: Application to dynamic earthquake triggering. *Geophys. Res. Lett.*, 42(22):9750–9757, November 2015.

[28] S Förster, M Konrad, and P Lindner. Shear thinning and orientational ordering of wormlike micelles. *Phys. Rev. Lett.*, 94(1):017803, January 2005.

[29] Chuyuan Fu, Qi Guo, Theodore Gast, Chenfanfu Jiang, and Joseph Teran. A polynomial particle-in-cell method. *ACM Transactions on Graphics (Proc. of SIGGRAPH Asia 2017)*, 36(6):222:1–12, 2017.

[30] C. Gallegos and J.M. Franco. Rheology of food, cosmetics and pharmaceuticals. *Curr. Opin. Colloid Interface Sci.*, 4(4):288–293, August 1999.

[31] Ming Gao, Andre Pradhana, Xuchen Han, Qi Guo, Grant Kot, Eftychios Sifakis, and Chenfanfu Jiang. Animating fluid sediment mixture in particle-laden flows. *ACM Transactions on Graphics (Proc. of SIGGRAPH 2018)*, 37(4):149:1–11, 2018.

[32] Ming Gao, Xinlei Wang, Kui Wu, Andre Pradhana, Eftychios Sifakis, Cem Yuksel, and Chenfanfu Jiang. Gpu optimization of material point methods. *ACM Transactions on Graphics (Proc. of SIGGRAPH Asia 2018)*, 37(6):254:1–12, 2018.

[33] Theodore F. Gast, Craig Schroeder, Alexey Stomakhin, Chenfanfu Jiang, and Joseph M. Teran. Optimization integrator for large time steps. *IEEE Transactions on Visualization and Computer Graphics*, 21(10):1103–1115, 2015.

[34] Johan Gaume, Theodore F. Gast, Joseph Teran, Alec van Herwijnen, and Chenfanfu Jiang. Dynamic anticrack propagation in snow. *Nature Communications*, 9:3047:1–10, 2018.

[35] D. B. Genovese, J. E. Lozano, and M. A. Rao. The rheology of colloidal and noncolloidal food dispersions. *Journal of Food Science*, 72(2):11–20, 2007.

[36] Alexander L Handwerger, Alan W Rempel, Rob M Skarbek, Joshua J Roering, and George E Hilley. Rate-weakening friction characterizes both slow sliding and catastrophic failure of landslides. *Proc. Natl. Acad. Sci. U. S. A.*, 113(37):10281–10286, September 2016.

[37] G. Heirman, L. Vandewalle, D. Van Gemert, and Ó. Wallevik. Integration approach of the couette inverse problem of powder type self-compacting concrete in a wide-gap concentric cylinder rheometer. *J. Non-Newtonian Fluid Mech.*, 150(2):93–103, April 2008.

[38] Malte Henkel, Haye Hinrichsen, and Sven Lübeck. *"Non-Equilibrium Phase Transitions Volume 1: Absorbing Phase Transitions"*. Springer, Dordrecht, 2008.

[39] H. Hinrichsen. "Non-equilibrium critical phenomena and phase transitions into absorbing states". **49**:815–958, 2000.

[40] Yuanming Hu, Yu Fang, Ziheng Ge, Ziyin Qu, Yixin Zhu, Andre Pradhana, and Chenfanfu Jiang. A moving least squares material point method with displacement discontinuity and two-way rigid body coupling. *ACM Transactions on Graphics (Proc. of SIGGRAPH 2018)*, 37(4):150:1–14, 2018.

[41] Douglas J. Jerolmack and Karen E. Daniels. Viewing earth's surface as a soft-matter landscape. *Nature Reviews Physics*, 1(12):716–730, October 2019.

[42] Chenfanfu Jiang, Theodore Gast, and Joseph Teran. Anisotropic elastoplasticity for cloth, knit and hair frictional contact. *ACM Transactions on Graphics (Proc. of SIGGRAPH 2017)*, 36(4):152:1–14, 2017.

[43] Chenfanfu Jiang, Craig Schroeder, Andrew Selle, Joseph Teran, and Alexey Stomakhin. The affine particle-in-cell method. *ACM Transactions on Graphics (Proc. of SIGGRAPH 2015)*, 34(4):51:1–10, 2015.

[44] Chenfanfu Jiang, Craig Schroeder, Andrew Selle, Joseph Teran, and Alexey Stomakhin. The affine particle-in-cell method. *ACM Transactions on Graphics*, 34(4):1–10, July 2015.

[45] Harry C. Jones and Eugene C. Bingham. Conductivity and viscosity of solutions of certain salts in mixtures of acetone with methyl alcohol, with ethyl alcohol and water. *American Chemical Journal*, 34:481–554, 1905.

[46] Takeshi Kawasaki and Ludovic Berthier. Macroscopic yielding in jammed solids is accompanied by a nonequilibrium first-order transition in particle trajectories. *Phys. Rev. E*, 94:022615, Aug 2016.

[47] James Kendall and Kenneth Potter Monroe. The viscosity of liquids. ii. the viscosity-composition curve for ideal liquid mixtures.1. *Journal of the American Chemical Society*, 39(9):1787–1802, 1917.

[48] J.M. Kim, D.J. Keffer, M. Kröger, and B.J. Edwards. Rheological and entanglement characteristics of linear-chain polyethylene liquids in planar couette and planar elongational flows. *J. Non-Newtonian Fluid Mech.*, 152(1):168–183, June 2008.

[49] Gergely Klár, Theodore Gast, Andre Pradhana, Chuyuan Fu, Craig Schroeder, Chenfanfu Jiang, and Joseph Teran. Drucker-prager elastoplasticity for sand animation. *ACM Transactions on Graphics (Proc. of SIGGRAPH 2016)*, 35(4):103:1–12, 2016.

[50] E. D. Knowlton, D. J. Pine, and L. Cipelletti. A microscopic view of the yielding transition in concentrated emulsions. *Soft Matter*, 10:6931–6940, 2014.

[51] William P. Krekelberg, Thomas M. Truskett, and Venkat Ganesan. Relationship between shear viscosity and structure of a model colloidal suspension. *Chem. Eng. Commun.*, 197(1):63–75, October 2009.

[52] Irvin M. Krieger and Thomas J. Dougherty. A Mechanism for Non - Newtonian Flow in Suspensions of Rigid Spheres. *Transactions of the Society of Rheology*, 3(1):137–152, 1959.

[53] Hitoshi Kumagai and Hitomi Kumagai. Physical properties of foods and effect of water on them V rheology and food engineering. *Japan Journal of Food Engineering*, 10(3):137–148, 2009.

[54] Lei Lan, Yin Yang, Danny Kaufman, Junfeng Yao, Minchen Li, and Chenfanfu Jiang. Medial IPC: Accelerated incremental potential contact with medial elastics. *ACM Transactions on Graphics*, 2021.

[55] Maxim O. Lavrentovich, Andrea J. Liu, and Sidney R. Nagel. Period proliferation in periodic states in cyclically sheared jammed solids. *Phys. Rev. E*, 96:020101, Aug 2017.

[56] E. L. Lederer. Zur theorie der viskosität von flüssigkeiten. *Kolloid Beihefte*, 34(5-9):270–338, 1931.

[57] Edan Lerner, Gustavo Düring, and Matthieu Wyart. A unified framework for non-brownian suspension flows and soft amorphous solids. *Proc. Natl. Acad. Sci. USA*, 109:4798, 2012.

[58] Felipe R Loyola, Waldyr de Lima e Silva, Luiz G C Campos, and Christian J L Hermes. Rheometric assessment and numerical simulation of steady-state and

periodic flows of fabric-water mixtures in household top-load washing machines. *Chem. Eng. Res. Des.*, 137:273–290, September 2018.

[59] Christopher W Macosko. *Rheology: Principles, Measurements, and Applications*. Wiley, 1996.

[60] T.G. Mason, J. Bibette, and D.A. Weitz. Yielding and flow of monodisperse emulsions. *Journal of Colloid and Interface Science*, 179(2):439 – 448, 1996.

[61] Thomas G Mezger. *The Rheology Handbook: 5th Edition*. Vincentz Network, 2020.

[62] Rebecca R Milczarek and Kathryn L Mccarthy. Relationship between the bostwick measurement and fluid properties. *J. Texture Stud.*, 37(6):640–654, December 2006.

[63] Takamasa Mori, Shohei Moriya Ma, Takuto Nakagawa, and Jun Ichiro Tsubaki. Measurement of apparent viscosity of various fluids by using B-Type and Vibration-Type viscometers. *Nihon Reoroji Gakkaishi*, 45(5):157–165, 2017.

[64] S. Mueller, E. W. Llewellin, and H. M. Mader. The rheology of suspensions of solid particles. *Proc. R. Soc. A*, 39:1201–1228, 2010.

[65] Kentaro Nagasawa, Kunimasa Miyazaki, and Takeshi Kawasaki. Classification of the reversible–irreversible transitions in particle trajectories across the jamming transition point. *Soft Matter*, 15(38):7557–7566, October 2019.

[66] Kentaro Nagasawa, Takayuki Suzuki, Ryohei Seto, Masato Okada, and Yonghao Yue. Mixing sauces: A viscosity blending model for shear thinning fluids. *ACM Transactions on Graphics*, 2019.

[67] Q. D. Nguyen and D. V. Boger. Measuring the Flow Properties of Yield Stress Fluids. pages 47–88, 1992.

[68] Katsuyoshi Nishinari, Mihaela Turcanu, Makoto Nakauma, and Yapeng Fang. Role of fluid cohesiveness in safe swallowing. *NPJ Sci Food*, 3:5, April 2019.

[69] James F. O'Brien, Adam W. Bargteil, and Jessica K. Hodgins. Graphical Modeling and Animation of Ductile Fracture. *ACM Transactions on Graphics*, 21(3):291–294, jul 2002.

[70] Anna Maria Pellegrino and Leonardo Schippa. A laboratory experience on the effect of grains concentration and coarse sediment on the rheology of natural debris-flows. *Environ. Earth Sci.*, 77(22):749, November 2018.

[71] Roberto Piazza. *Soft Matter (The stuff that dreams are made of)*. Springer, Dordrecht, 2010.

[72] D. J. Pine, J. P. Gollub, J. F. Brady, and A. M. Leshansky. "Chaos and threshold for irreversibility in sheared suspensions". **438**:997–1000, 2005.

[73] Andre Pradhana, Theodore Gast, Gergely Klár, Chuyuan Fu, Joseph Teran, Chenfanfu Jiang, and Ken Museth. Multi-species simulation of porous sand and water mixtures. *ACM Transactions on Graphics (Proc. of SIGGRAPH 2017)*, 36(4):105:1–11, 2017.

[74] Daniel Ram, Theodore Gast, Chenfanfu Jiang, Craig Schroeder, Alexey Stomakhin, Joseph Teran, and Pirouz Kavehpour. A material point method for viscoelastic fluids, foams and sponges. In *Proceedings of the 14th ACM SIGGRAPH / Eurographics Symposium on Computer Animation*, SCA '15, pages 157–163. ACM, 2015.

[75] A. Rao. *Rheology of Fluid, Semisolid, and Solid Foods Princiles and Application.* Springer, 2014.

[76] Bo Ren, Ben Xu, and Chenfeng Li. Unified particle system for multiple-fluid flow and porous material. *ACM Transactions on Graphics*, 40(4):1–14, July 2021.

[77] Michel (Sr.) Roegiers and Lucien Roegiers. La viscosité des mélanges de fluides normaux. 1946.

[78] Michael Rusin. The structure of nonlinear blending models. *Chemical Engineering Science*, 30(8):937–944, 1975.

[79] Ma Carmen Sánchez, Concepción Valencia, Críspulo Gallegos, Ascensión Ciruelos, and Antonio Latorre. Influence of processing on the rheological properties of tomato paste. *J. Sci. Food Agric.*, 82(9):990–997, July 2002.

[80] Carl F. Schreck, Robert S. Hoy, Mark D. Shattuck, and Corey S. O'Hern. Particle-scale reversibility in athermal particulate media below jamming. *Phys. Rev. E*, 88:052205, Nov 2013.

[81] Ryohei Seto, Romain Mari, Jeffrey F. Morris, and Morton M. Denn. The Essential Role of Frictional Contact in Shear Thickening. *Japanese Journal of Multiphase Flow*, 28(3):296–303, 2014.

[82] J. C. Simo. A Framework for Finite Strain Elastoplasticity Based on Maximum Plastic Dissipation and the Multiplicative Decomposition: Part I. Continuum Formulation. *Computer Methods in Applied Mechanics and Engineering*, 66(2):199–219, feb 1988.

[83] Juan C. Simo and Thomas J. R. Hughes. *Computational Inelasticity.* Springer, 1998.

[84] Alexey Stomakhin, Craig Schroeder, Lawrence Chai, Joseph Teran, and Andrew Selle. A material point method for snow simulation. *ACM Transactions on Graphics (Proc. of SIGGRAPH 2013)*, 32(4):102:1–10, 2013.

[85] Alexey Stomakhin, Craig Schroeder, Chenfanfu Jiang, Lawrence Chai, Joseph Teran, and Andrew Selle. Augmented MPM for phase-change and varied materials. *ACM Transactions on Graphics (Proc. of SIGGRAPH 2014)*, 33(4):138:1–11, 2014.

[86] Haozhe Su, Tao Xue, Chengguizi Han, Chenfanfu Jiang, and Mridul Aanjaneya. A unified second-order accurate in time MPM formulation for simulating viscoelastic liquids with phase change. *ACM Transactions on Graphics*, 2021.

[87] Deborah Sulsky, Zhen Chen, and Howard L. Schreyer. A particle method for history-dependent materials. *Computer methods in applied mechanics and engineering*, 118(1):179–196, 1994.

[88] Deborah Sulsky, Shi-Jian Zhou, and Howard L. Schreyer. Application of a particle-in-cell method to solid mechanics. *Computer Physics Communications*, 87(1-2):236–252, 1995.

[89] Gipsy Tabilo-Munizaga and Gustavo V Barbosa-Cánovas. Rheology for the food industry. *J. Food Eng.*, 67(1):147–156, March 2005.

[90] Anette K Thybo, Iben E Bechmann, and Kirsten Brandt. Integration of sensory and objective measurements of tomato quality: quantitative assessment of the effect of harvest date as compared with growth medium (soilversus rockwool), electrical conductivity, variety and maturity. *J. Sci. Food Agric.*, 85(13):2289–2296, October 2005.

[91] Elsen Tjhung and Ludovic Berthier. Discontinuous fluidization transition in time-correlated assemblies of actively deforming particles. *Phys. Rev. E*, 96:050601, Nov 2017.

[92] Martin van Hecke. Jamming of soft particles: geometry, mechanics, scaling and isostaticity. *J. Phys. Condens. Matter*, 22(3):033101, January 2010.

[93] H. A. Vinutha and Srikanth Sastry. "Disentangling the role of structure and friction in shear jamming". **12**:578–583, 2016.

[94] H. A. Vinutha and Srikanth Sastry. Geometric aspects of shear jamming induced by deformation of frictionless sphere packings. *Journal of Statistical Mechanics: Theory and Experiment*, 2016(9):094002, 2016.

[95] Xinlei Wang, Minchen Li, Yu Fang, Xinxin Zhang, Ming Gao, Min Tang, Danny M. Kaufman, and Chenfanfu Jiang. Hierarchical optimization time integration for cfl-rate mpm stepping. *ACM Transactions on Graphics*, 2020.

[96] Xinlei Wang, Yuxing Qiu, Stuart R Slattery, Yu Fang, Minchen Li, Song-Chun Zhu, Yixin Zhu, Min Tang, Dinesh Manocha, and Chenfanfu Jiang. A massively parallel and scalable multi-GPU material point method. *ACM Transactions on Graphics*, 39(4):30:1–30:15, July 2020.

[97] C. R. Wildemuth and M. C. Williams. Viscosity of suspensions modeled with a shear-dependent maximum packing fraction. *Rheologica Acta*, 23(6):627–635, November 1984.

[98] R. W. Williams. Determination of viscometric data from the brookfield R.V.T. viscometer. *Rheologica Acta*, 18(3):345–359, May 1979.

[99] Joshuah Wolper, Yu Fang, Minchen Li, Jiecong Lu, Ming Gao, and Chenfanfu Jiang. CD-MPM: continuum damage material point methods for dynamic fracture animation. *ACM Transactions on Graphics*, 2019.

[100] Joshuah Wolper, Ming Gao, Martin P Lüthi, Valentin Heller, Andreas Vieli, Chenfanfu Jiang, and Johan Gaume. A glacier–ocean interaction model for tsunami genesis due to iceberg calving. *Commun Earth Environ*, 2(1), December 2021.

[101] Joel Wretborn, Rickard Armiento, and Ken Museth. Animation of crack propagation by means of an extended multi-body solver for the material point method. *Computers and Graphics*, 69(C):131–139, 2017.

[102] Yonghao Yue, Breannan Smith, Christopher Batty, Changxi Zheng, and Eitan Grinspun. Continuum foam: A material point method for shear-dependent flows. *ACM Transactions on Graphics*, 34(5):160:1–20, 2015.

[103] Yonghao Yue, Breannan Smith, Peter Yichen Chen, Maytee Chantharayukhonthorn, Ken Kamrin, and Eitan Grinspun. Hybrid grains: adaptive coupling of discrete and continuum simulations of granular media. *ACM Transactions on Graphics (Proc. of SIGGRAPH Asia 2018)*, 37(6):283:1–19, 2018.

Appendix A

Appendix

6 章に関連する内容であり，5 年以内に雑誌等で刊行予定のため、非公開。